EFFECT OF FIBER DIAMETER ON STRESS TRANSFER AND INTERFACIAL DAMAGE IN FIBER REINFORCED COMPOSITES

by

William Matthew Peterson

A thesis submitted in partial fulfillment
of the requirements for the degree

of

Master of Science

in

Mechanical Engineering

MONTANA STATE UNIVERSITY
Bozeman, Montana

July 2011

APPROVAL

of a thesis submitted by

William Matthew Peterson

This thesis has been read by each member of the thesis committee and has been found to be satisfactory regarding content, English usage, format, citation, bibliographic style, and consistency and is ready for submission to The Graduate School.

Dr. Christopher H. M. Jenkins

Approved for the Department of Mechanical Engineering

Dr. Christopher H. M. Jenkins

Approved for The Graduate School

Dr. Carl A. Fox

STATEMENT OF PERMISSION TO USE

William Matthew Peterson

July 2011

ACKNOWLEDGEMENTS

First and foremost, I would like to acknowledge the inspiration and encouragement that I received from my family. Thank you so much for being my well-spring of support, my shade-tree when I needed it, and for sharing with me your sense of humor.

Many thanks go to my major professor and advisor, Dr. Chris Jenkins, who has been exceedingly patient and trusting in this work, has provided me with a great learning environment, and has given me an excellent introduction into both the practice and philosophy of the engineering profession. The efforts of my two other committee members, Dr. Dave Miller and Dr. Ladean McKittrick, have also provided me with wonderful insights into aspects of this research that I might not have otherwise considered. I would also like to acknowledge Dr. Kyeongsik Woo and Dr. Awlad Hossain for their thoughtful review. I truly enjoyed having the chance to bounce ideas back and forth with each of the excellent people I have been able to work with – including my committee members, other faculty, staff, and fellow students.

Finally, I want to thank whoever invented coffee, particularly espresso – without which this work would not have been possible. Of course, this thanks extends to all the people who made me coffee over the last several months.

TABLE OF CONTENTS

TABLE OF CONTENTS - CONTINUED

LIST OF TABLES

LIST OF FIGURES

LIST OF FIGURES - CONTINUED

Figure Page

LIST OF FIGURES - CONTINUED

LIST OF FIGURES - CONTINUED

Figure Page

ABSTRACT

In this work, the effect of fiber diameter upon the strength, stiffness, and damage tolerance of a fiber-reinforced polymer composite laminate structure was investigated. Three cases were considered, in which the fiber diameters of 16, 8, and 4 μm were used. A fiber volume fraction of 32% was assumed in each model. Micromechanical, shear-lag, and progressive damage analyses were performed using finite element models of the structure, which was subjected to tensile loading in the fiber direction. Fiber-matrix load transfer efficiencies and the stress distributions near broken fibers within the composite structure were investigated and results compared for each fiber diameter. In addition, the effect of fiber diameter upon the initiation and evolution of fiber-matrix interfacial damage and debonding was studied using cohesive interface elements. For a specified volume fraction and load condition, as the fiber diameter was decreased the load transfer efficiency and effective stiffness of the broken fiber model increased. Also, as the fiber diameter was decreased, the initiation of damage at the fiber-matrix interface occurred at greater stresses and the subsequent growth of damage was less extensive. These results indicate that, for the same total mass, the performance and damage tolerance of composite materials may be enhanced simply by using smaller diameter fibers.

INTRODUCTION

Background

Composite material technology is based on the simple concept that the bulk response of a heterogeneous material may be modified by selecting different combinations of the component materials. This insight has led to remarkable developments in the ability to obtain excellent physical and mechanical properties in engineered composite materials through the careful selection of constituent materials, as well as their form, volume fraction, and geometric arrangement. Consequently, modern composites may often be tailored for a specific application, and are found in a growing number of important roles in industry today.

As high performance advanced composites become increasingly relevant and complex, improvements in their design, manufacture, and mechanical characterization are continually sought. In particular, the design and analysis of composite materials using predictive models has seen significant development. During the last 50 years, research has expanded from the prediction of homogenized properties of a composite, to address the important problem of damage initiation and evolution [**1**].

Motivation

In fiber-reinforced polymer (FRP) composites, it is generally accepted that the fiber-matrix interface is critical to the overall mechanical properties of the material [**2**,**3**,**4**], providing the means through which loads are transferred from matrix to fiber. The strength and stiffness of the interfacial bond, as well as the integrity of the fiber-matrix boundary, are essential factors affecting the composite material's overall performance and resistance to damage.

Ostensibly, as the total effective (bonded) fiber-matrix interfacial surface area increases, loads may be more efficiently redistributed from fiber to fiber. Such an increase in the surface area at the fiber-matrix interface may also potentially compensate for broken fibers and imperfect bonding at the fiber-matrix boundary. It is with this basic concept that the current work is motivated.

Within a specified volume containing continuous fiber reinforcements, there are two means by which such an increase in fiber-matrix interfacial surface area may be achieved:

A. Increasing the fiber volume fraction while keeping the fiber diameter constant;

B. Decreasing the fiber diameter while keeping the fiber volume fraction constant.

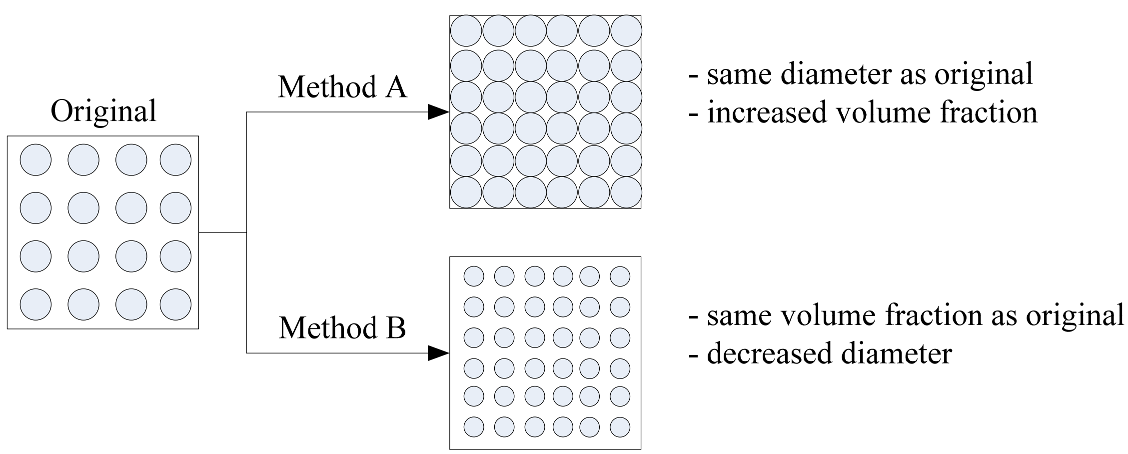

Figure 1. Two methods to increase the interfacial surface area within a specified volume.

The key differences between these two methods are next demonstrated through a brief example. Before modification, consider a fiber-reinforced composite originally composed of equal parts by volume of fiber and matrix materials, i.e., the fiber volume fraction is $V_{f0} = 50\%$. Let the typical fiber diameter be $D_0 = 25$ μm. Assuming the fibers are continuous and there are no internal voids, using Equations 1-3 it can be found that in one cubic meter (where the height h, width w, and length L are equal) the total interfacial surface area is $A_{s0} = 80\ 000$ m^2.

$$V_f = \frac{N_f\ \pi\ D^2\ L}{4\ h\ w\ L} = \frac{N_f\ \pi\ D^2}{4\ L^2} \qquad \text{Eq. (1)}$$

$$N_f = \frac{4\ V_f L^2}{\pi\ D^2} \qquad \text{Eq. (2)}$$

$$A_s = N_f \pi\ D\ L = \frac{4\ V_f\ L^3}{D} \qquad \text{Eq. (3)}$$

Therefore, the surface area is proportional to V_f/D.

Now, consider Method A (or, the "V_f-scaling method") from above. While keeping the fiber diameter constant, any increase in the number of fibers (N_f) will increase the total interfacial surface area within the volume (L^3). For instance, if maintaining $D_A = D_0 = 25$ μm while increasing the number of fibers in the volume such that the fiber volume fraction becomes $V_{fA} = 75\%$, the new composite will have a fiber-matrix interfacial surface area of $A_{sA} = 120\ 000$ m^2.

Alternatively, in Method B (or, the "fiber-scaling method") the fiber volume fraction is held constant at $V_{fB} = V_{f0} = 50\%$ while the typical fiber diameter decreases. For comparison, in order to obtain a fiber-matrix surface area of $A_{sB} = A_{sA} = 120\ 000$ m^2, the fiber diameter must decrease to approximately $D_B = 16.7$ μm. As a natural consequence of maintaining a constant fiber volume fraction while decreasing the fiber diameter, the number of fibers in the composite structure must increase. Accordingly, the amount of fiber-matrix interfacial area increases while the total mass of the composite remains the same. In fact, as shown in Equations 4-8, if *N* fibers of diameter *D* are replaced by *n* smaller fibers of diameter *d* in a cubic volume with side lengths *L* while the fiber volume fraction V_f remains constant, then the interfacial surface area A_{s2} increases by a factor of $(n/N)^{1/2}$ over the original area A_{s1}.

Using

$$V_f = \frac{N\,\pi\,D^2}{4\,L^2} = \frac{n\,\pi\,d^2}{4\,L^2} \qquad \text{Eq. (4)}$$

$$\therefore\ d = D\,\sqrt{N/n} \qquad \text{Eq. (5)}$$

Also

$$A_{s1} = N\,\pi\,D\,L \qquad \text{Eq. (6)}$$

$$\therefore\ A_{s2} = n\,\pi\,D\,L\,\sqrt{N/n} = \frac{n}{N}\sqrt{\frac{N}{n}}\,A_{s1} \qquad \text{Eq. (7)}$$

Thus,

$$A_{s2} = \sqrt{n/N}\,A_{s1} \qquad \text{Eq. (8)}$$

Note that in either case, the number of fibers must increase. However, fiber reinforcements often have higher densities than matrices; therefore, the disadvantage of the first method is that as V_f increases, the total mass of the composite material also increases. This is not an issue in the second method since V_f does not change. The results from this comparison are summarized in Table 1 using properties typical for an E-glass/epoxy fiber-reinforced composite, assuming a total volume of 1 m^3.

Table 1. Comparison of methods to increase fiber-matrix interfacial surface area.

Specimen	V_f ,%	D, µm	A_s , m^2	N_f	Mass*, kg
Original	50	25.0	80 000	1.02 E9	1850
A	75	25.0	120 000	1.53 E9	2175
B	50	16.7	120 000	2.28 E9	1850

At the present time, typical glass fibers are commercially produced with diameters ranging from 4-25 µm [**5**]. Therefore, when using a diameter of 4 µm the total interfacial surface area becomes approximately 500 000 m^2, an increase of 525% over the original area.

Consider also the rate at which the surface area may increase for each model. From Equation 2, we can see that if the fiber diameter (D) is constant while the volume fraction (V_f) varies, then N is a linear function of V_f. On the other hand, if D varies while V_f is constant, then N is proportional to $1/D^2$ and becomes exponentially large as D becomes small. This is clearly shown in Figures 2 and 3 below.

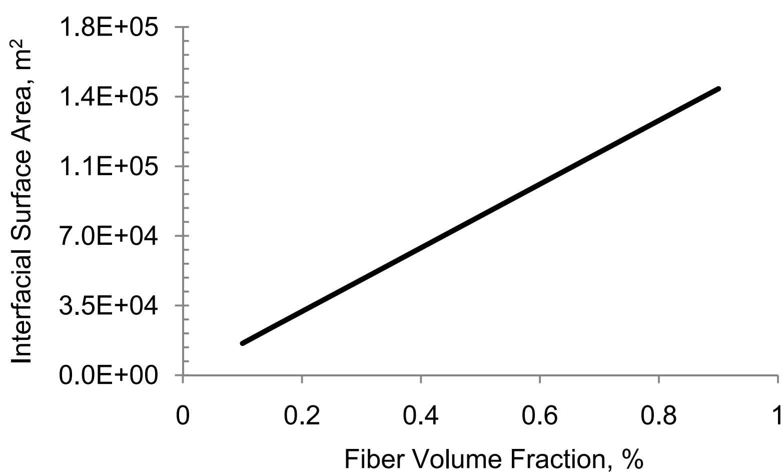

Figure 2. In Method A the interfacial surface area is a linear function of fiber volume fraction. Results are shown for a constant fiber diameter of D = 25 µm.

* E-glass fiber: density = 2500 kg/m^3, Epoxy matrix: density = 1200 kg/m^3 [**2**]

In Method A the interfacial surface area increases linearly as a function of the fiber volume fraction, as shown in Figure 2. In Method B, however, the interfacial surface area increases exponentially with decreases in the fiber diameter, as shown in Figure 3.

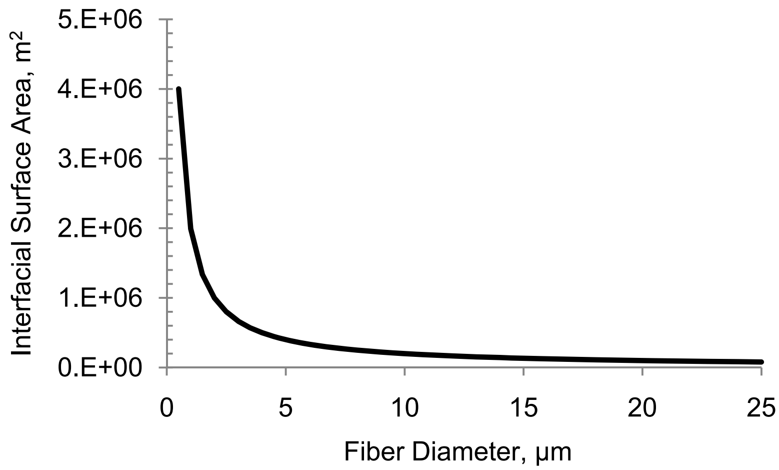

Figure 3. In Method B the interfacial surface area is an exponential function of fiber diameter. Results are shown for a constant fiber volume fraction of $V_f = 50\%$. Note the rapid increase once the diameter is less than 10 μm.

Objectives

From the preceding discussion, it can be seen that an increase in the fiber-matrix interfacial surface area may be accomplished within a specified volume by reducing the fiber diameter while the fiber volume fraction is held constant (the "fiber scaling" method). The obvious benefit from the fiber scaling method is that, for a given fiber volume fraction, there is no simultaneous increase in mass as the interfacial area increases.

Although extensive research exists in the literature regarding fiber-reinforced composite materials and their behavior, at this time very little has been documented with respect to the effect of fiber diameter upon fiber-matrix load transfer characteristics and the overall toughness of the composite. As discussed in further sections, it also appears that most micromechanical models in current use are, in fact, based upon fiber volume fraction considerations only. Therefore, it is the goal of this work to provide a theoretical investigation into fiber scaling effects.

Primary Objectives

The primary objectives of this research are to investigate the effect of fiber diameter and the total fiber-matrix interfacial surface area upon the:

1. Composite material stiffness;
2. Fiber-matrix load transfer efficiency;
3. Fiber-matrix stress distributions;
4. Interfacial strength and damage resistance.

Secondary Objectives

In order to accomplish Primary Objective 4, an appropriate method of modeling the initiation and evolution of damage is needed. Therefore, an important part of this research is to:

5. Demonstrate the use of the cohesive zone model (CZM) to analyze fiber-matrix interfacial damage and debonding.

The CZM approach is a numerical representation of the progressive damage and failure of a material implemented using the finite element method (FEM). Using this method, cohesive elements are placed within the FE mesh at the fiber-matrix interface, allowing the model to simulate the onset and evolution of interfacial damage at critical loads – thus combining micromechanics and progressive damage modeling at the constituent level in a composite material.

Methods

In micromechanical approaches, the essential details of a composite microstructure are considered, e.g., the constituent phases, their form, volume fraction, geometric arrangement, and bonding characteristics. In one successful micromechanical technique, numerical models of an appropriate representative subset of the composite material are used to analyze the local effects of stress and strain. Because microstructural detail is retained in this approach, the discrete effects of deformation and damage upon the matrix and reinforcing phases may be described, and different damage mechanisms may be monitored – such as fiber-matrix interactions and interfacial debonding in fiber-reinforced composites.

In order to achieve the objectives given above, in this work a number of micromechanical finite element (FE) analyses of an FRP composite laminate structure are presented. Importantly (and in contrast to many typical micromechanical methods), the representative subvolume dimensions, geometry, and structural boundary conditions must be the same in each case. Three cases are considered, in which the fiber diameters of 16, 8, and 4 μm are used. In each case, a fiber volume fraction of 32% is ensured by adjusting the fiber diameter and the number of fibers as required, within a well-defined volume in the manner demonstrated by Method B in the example above. Fiber-matrix load transfer efficiencies and stress distributions near broken fibers within the composite structure are investigated. In addition, the effect of fiber diameter upon the initiation and evolution of fiber-matrix interfacial damage and debonding is studied using cohesive interface elements. Results are compared for each fiber diameter.

Numerical analysis has become the dominant method for modeling the failure behavior of composite materials, and allows the treatment of detailed and complex microstructures. In particular, the use of the finite element method (FEM) has become widespread, due to its powerful ability to obtain approximate solutions to field problems (such as described by differential or integral expressions) where analytical solutions may not be possible. It is not in the scope of this work to fully describe the FEM or procedures used in finite element analysis (FEA). Interested readers are referred to works by other authors such as by Cooke et al. [**6**]. However, a brief description is useful in the following sections. Therefore, briefly stated, in the FEM a continuous field problem described by differential or integral expressions is discretized into a mesh of smaller elements of a finite size, connected at their boundaries by nodes. The piecewise solution to the field problem for the unknown field quantity (such as displacement resulting from a structural load) at each node in the mesh is numerically obtained by solving a system of algebraic equations – thus, an approximation for the spatial variation of the field solution is achieved element-by-element. As mentioned, FEA gives an approximation to the “exact” solution obtained by the calculus of the differential/integral problem. Generally, this approximate solution improves as more elements are added to the mesh. In this work, an appropriate conceptual subvolume of the composite structure is chosen, which is then further discretized into a mesh of smaller elements.

THEORETICAL BACKGROUND

Composite Materials Overview

Biological structural composite materials such as wood, bone, and shell are ubiquitous in nature and multifunctional in purpose. Similarly, modern composite materials are commonly tailored in an attempt to achieve the desired physical and mechanical behavior, through the combination of two or more discrete constituent phases. By convention, composites are classified either by the type and geometry of the reinforcement, or by the type of matrix [**2**,**7**,**8**]. Composites classified by matrix type include: polymer matrix composites (PMCs), ceramic matrix composites (CMCs); metal matrix composites (MMCs); and carbon/carbon matrix composites (CCCs). Figure 4 illustrates three main types of reinforcements: particles, flakes, and fibers.

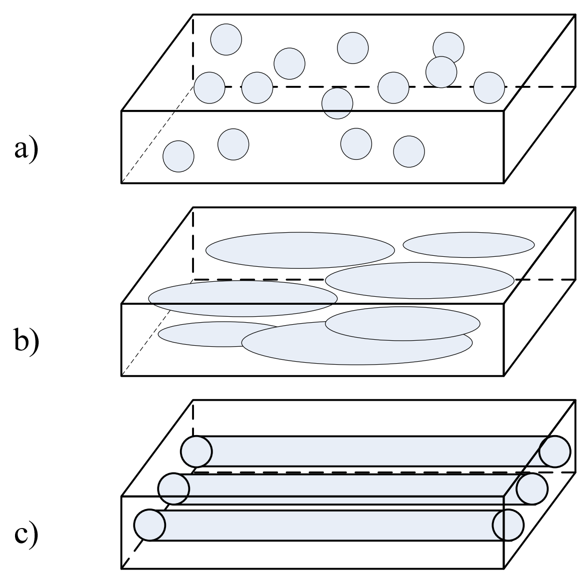

Figure 4. Three main types of composite reinforcements: a) particles, b) flakes, and c) fibers.

Various subclasses of composite reinforcements are also possible. Each designation and subclass helps to identify the different mechanical properties and manufacturing techniques that are associated with each fiber arrangement. For example, in fiber-reinforced composites, the fibers may be short (in discontinuous, random arrangements), long (in continuous, unidirectional arrangements), or form a textile weave. In addition, hybrid composites incorporate more than one type of reinforcement.

Fiber-Reinforced Polymer Composites

The most common advanced composites are polymer matrix composites (PMCs) reinforced with continuous thin diameter fibers [**8**], also known as fiber-reinforced polymer (FRP) composites. The fibers are generally strong and stiff along the fiber axis, and carry the majority of structural loads. The matrix is typically a tougher material with low mechanical properties, and serves to keep the fiber reinforcements aligned, to redistribute the load among the fibers, and to protect the fibers from environmental exposure. FRP laminates are made by assembling successive layers of thin laminae, or plies, together. The mechanical properties of each lamina are directionally-dependent on the fiber orientation – usually, multi-directional stiffness is achieved in laminates by using different fiber orientations for each layer, or by employing textile weaves [**8**].

Initially developed for use in the aerospace industry, advanced composites using fiber-reinforced matrices offer considerable advantages relative to unreinforced monolithic materials in structural applications where high strength, stiffness, low weight, and fatigue resistance are important factors. Such materials now play an important role in many other fields, such as the wind energy, automotive, marine, and sports equipment industries [**2**,**8**].

Micromechanics of Composite Materials

Composite materials are considered to be macroscopically heterogeneous combinations of discrete constituent materials that have been bonded together. Although they act in concert to produce the overall material behavior, the constituents retain their identities. As a result, the local properties of a composite change from point to point, depending on which phase the point is located in. This is in contrast to microscopic combinations such as found in metal alloys or ceramics, which to a first approximation are usually considered to be homogeneous [**2**,**8**]. This distinction is an important characteristic of composite materials – indeed, the mechanical performance of a composite is the result of complex interactions at the constituent level. For this reason, the design, analysis, and mechanical characterization of composite materials is generally much more complex than for monolithic materials, and has been a subject of extensive research in recent decades.

Micromechanics is the study of the relations between the properties of the constituents and the effective properties resulting from their specific combination. As such, micromechanical models are based on known properties (such as the individual mechanical behavior of the reinforcement and matrix phases, their volume fractions and geometric arrangement) as well as assumptions regarding the interactions between the constituent materials when under loading. In this capacity, micromechanics may be used to speed the design and development of new composite materials by identifying promising combinations before manufacturing and physical characterization is undertaken [**9**].

Homogenization Theory

The microstructural geometry of most composite materials is inherently complex. Consider the cross section of a typical glass/epoxy composite laminate as seen in the scanning electron microscope (SEM) images shown in Figures 5-7. First, Figure 5 shows the geometric arrangement of fiber bundles in each lamina, as well as several voids. Next, in Figure 6 both the individual strands and fiber bundles are apparent at an intermediate magnification; and in Figure 7 the arrangement of individual fiber strands within a fiber bundle are shown.

At this microstructural level, micromechanical models allow the determination of local stresses at each point and within each phase of the composite. Such micromechanical stress analyses are useful in order to investigate local failure modes before they might be detected on a macro-scale. In most engineering structural analyses, however, the response of a macro-scale structure is of practical interest. This presents conflicting requirements: on one hand, mechanical analyses of composite materials without attention to the microstructure have limited ability to predict the material behavior [**10**]. On the other hand, the direct analysis of a macroscopic composite structure incorporating an exact representation of the material's microstructure is not currently possible by either analytical or numerical methods. To overcome this difficulty, the average response of the constituents taken within an appropriate volume at the microscale may then be used to predict the material behavior of a structure on the macroscale. This volume-averaging technique is called homogenization.

Although the stresses and strains at the microstructural level are not uniform as a result of the different constituent material behaviors, in homogenization theory the volume assumed by a micromechanical model can be replaced by an equivalent homogeneous material with behavior described by the averaged responses of the constituents. Therefore, the effective, or homogenized, properties obtained from a micromechanical analysis are essential in the design and analysis of a composite structure at the macroscale.

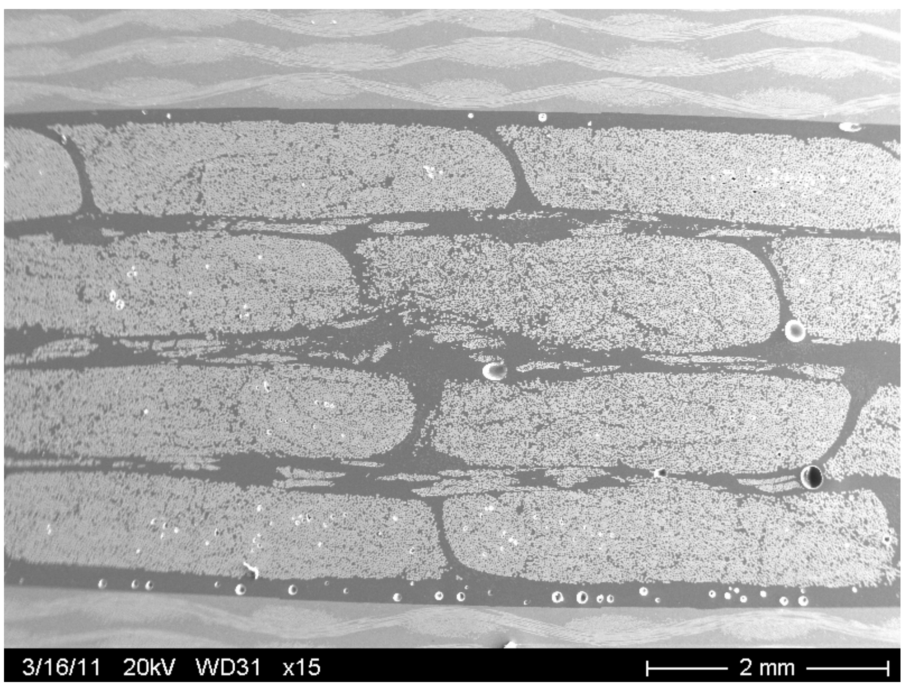

Figure 5. Cross section of typical $[45/45]_S$ glass/epoxy laminate†. SEM x15.

† Images: Montana State University, Composite Technologies Research Group, 2011.

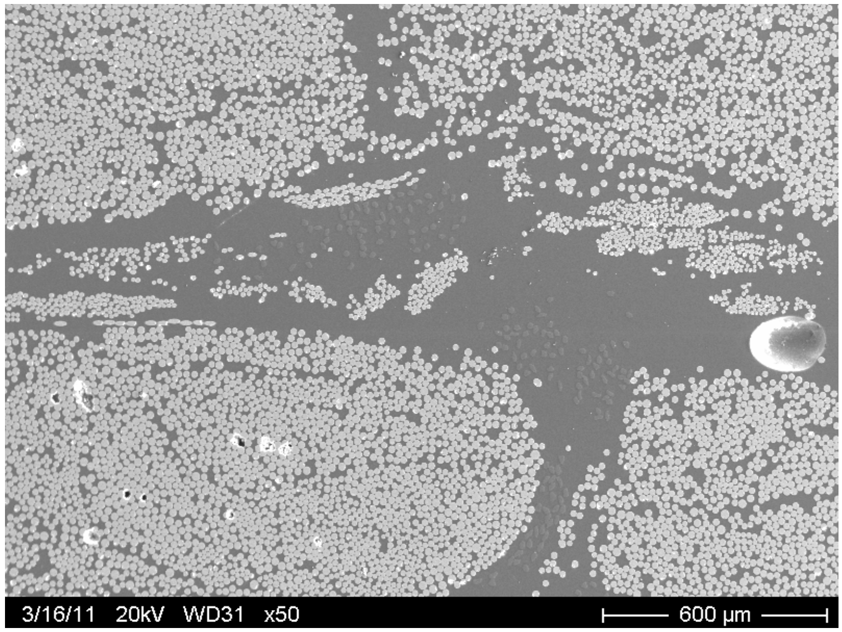

Figure 6. Cross section of typical $[45/45]_S$ glass/epoxy laminate‡. SEM x50.

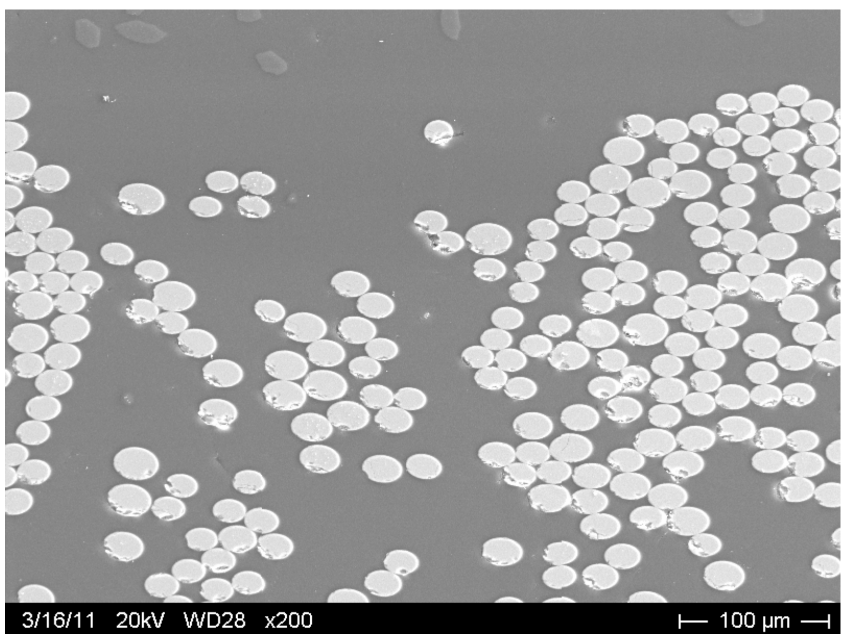

Figure 7. Unidirectional E-glass fibers in Hexion resin epoxy†. SEM x200.

‡ ,† Images: Montana State University, Composite Technologies Research Group, 2011.

In an FRP composite, for example, using homogenized properties it is then possible to obtain the average stresses within a lamina, without the need to keep track of the behavior of each fiber and fiber-matrix interaction. At this point, the fundamental difference between a homogenized lamina and most other monolithic materials is the high level of anisotropy manifested in the material properties; this directional dependence is due to the orientation of the load bearing fiber-reinforcements. In a laminate, each lamina may be associated with different homogenized properties and is assumed to behave as a distinct homogeneous material. In composite laminate models, such as the Classical Lamination Theory (CLT), the interaction of each layer in a laminate then becomes possible, and composite structural mechanics may be more easily undertaken.

Microstructural Representations

When the local micromechanical behavior of a composite material is of interest the actual geometric arrangement of the fibers within the matrix must be accounted for. This is especially the case when the initiation and evolution of damage at the constituent level is of concern. In order to avoid modeling all of the microstructural detail and conserve computational resources, micromechanical idealizations are commonly used in order to represent the essential microstructural details of a composite material. Such efforts are based on the assumption that models using an appropriate geometric representation and associated boundary conditions exhibit the mechanical behavior of the macroscopic material.

As discussed by Pindera et al. [**9**], the analysis of spatially uniform periodic composite materials may be grouped into two categories based on different geometric representations of the composite microstructure, each associated with different boundary conditions (BCs):

1. The Representative Volume Element (RVE), as shown in Figure 8a;
2. The Repeating Unit Cell (RUC), as shown in Figure 8b.

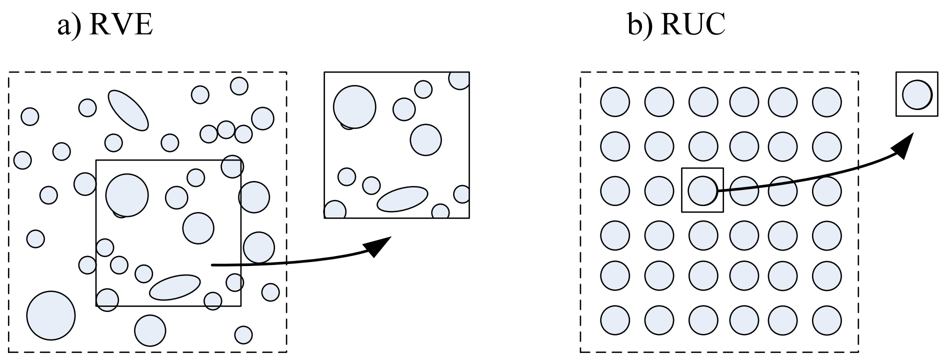

Figure 8. (a) The RVE microstructural representation characterizes the statistical distribution of a composite; (b) the RUC microstructural representation assumes a periodic microstructure, and can be small relative to the RVE.

These concepts and terms are sometimes used interchangeably in the literature, leading to some unfortunate confusion regarding the application of appropriate boundary conditions (for a detailed discussion see the works of Li [**11**,**12**] or Drago and Pindera [**13**], for example). Therefore, it is important to correctly identify each representation and establish their usefulness for the current research.

<u>The Representative Volume Element</u>. In the RVE, homogenization of material properties or microstructural stress analysis takes place over the smallest statistically representative sample of the material at large, which contains the same fiber and matrix volume fractions with the same distributions as the macroscopic material. This

representation is based on the assumption that the application of homogeneous traction and homogeneous displacement boundary conditions produce equivalent behavior and homogenized properties. The homogeneous displacement and homogeneous traction BCs are given in Equation 9 and 10, respectively.

$$u_i(\Sigma) = \varepsilon_{ij}^0 \, x_j \quad \text{where } x_j \in \Sigma \qquad \text{Eq. (9)}$$

$$T_i(\Sigma) = \sigma_{ij}^0 \, n_j \quad \text{where } n_j \in S \qquad \text{Eq. (10)}$$

In Equation 9, $u_i(\Sigma)$ are the displacement components applied to the boundary surface Σ at the location x_j – with the corresponding nominal strain field ε_{ij}^0; similarly, in Equation 10, $T_i(\Sigma)$ are the applied traction components – with the corresponding nominal stress field σ_{ij}^0.

In the RVE concept, macroscopically uniform displacement and traction BCs are applied in order to produce average strains ($\bar{\varepsilon}_{ij}$) and stresses ($\bar{\sigma}_{ij}$) in the micromechanical model – which are the same as the nominal, uniform strains (ε_{ij}^0) and stresses (σ_{ij}^0) that are produced when they are applied to an equivalent homogenized material [**9**]. If this assumption is satisfied, then the representative volume element experiences boundary deformations like an equivalent homogeneous material and the RVE characterization of the composite microstructure is valid.

In other words, the application of uniform displacement BC $u_i(\Sigma)$ upon a homogeneous material and the corresponding uniform strain field ε_{ij}^0 produces a uniform stress field σ_{ij}^0. In linear elastic homogeneous materials the stress and strain fields are related by the constitutive stiffness tensor C_{ijkl}, which is expressed by Hooke's Law, as in Equation 11.

$$\sigma_{ij}^{0} = C_{ijkl}\varepsilon_{kl}^{0} \qquad \text{Eq. (11)}$$

The reverse also holds, such that uniform traction boundary conditions and the corresponding uniform stress field produces a uniform strain field, as related by Hooke's Law and the inverse of the stiffness tensor (that is, the compliance tensor $S_{ijkl} = \left[C_{ijkl}\right]^{-1}$). Since the stiffness and compliance tensors are invertible, then the stress and strain fields are thus related and the moduli are independent of the BC type, and the strain energy in the homogeneous material can be expressed as in Equation 12 [**13**].

$$U = \frac{1}{2}\sigma_{ij}^{0}\varepsilon_{ij}^{0} \qquad \text{Eq. (12)}$$

In heterogeneous materials, the homogenized (effective) constitutive stiffness and compliance tensors replace the homogeneous ones, i.e., $C_{ijkl} \to C_{ijkl}^{*}$ and $S_{ijkl} \to S_{ijkl}^{*}$. If $S_{ijkl} \to \left[C_{ijkl}^{*}\right]^{-1}$, then the same homogenized moduli are obtained whether displacement or traction BCs are applied to the RVE . As a practical matter, however, this equivalence is usually only achieved as the number of inclusions becomes large [**9**,**14**], and as the size of the inclusions become small compared to the RVE boundary. As proposed by Hill [**15**], the equivalence of loading type may be accomplished by ensuring that the strain energies induced by homogenous traction or homogeneous displacement boundary conditions are essentially the same, such as in Equation 13.

$$\frac{1}{2}\sigma_{ij}^{0}\varepsilon_{ij}^{0} \cong \frac{1}{2}\bar{\sigma}_{ij}^{T}\bar{\varepsilon}_{ij} \cong \frac{1}{2}\bar{\sigma}_{ij}\bar{\varepsilon}_{ij}^{u} \qquad \text{Eq. (13)}$$

where:

$\bar{\sigma}_{ij}^{T}$ = average stresses induced by homogeneous traction boundary conditions

$\bar{\varepsilon}_{ij}^{u}$ = average strains induced by homogeneous displacement boundary conditions

With a sufficient number of inclusions, the homogenized properties calculated from the RVE analysis asymptotically converge upon a single value [**9**,**13**,**14**]. Therefore, while small in comparison to a full model attempting the direct analysis of a macroscopic composite structure, typical RVEs are still quite large and generally computationally intensive. In addition, several candidate RVEs may need to be tested before equivalence is achieved.

The Repeating Unit Cell. Alternatively, the microstructure of a composite material may be idealized as a periodic array of inclusions, as was illustrated in Figure 8b. In the RUC, homogenization of material properties or microstructural stress analysis takes place over the smallest element of a periodic microstructure which serves as the basic building block for the material through replication [**9**]. Unlike an RVE, an RUC is valid using any geometry and number of inclusions, provided the contents may be geometrically replicated to reproduce a periodic microstructure. Because each RUC in the array is identical, the response of any single subvolume to a load is identical to that of the entire array. However, it is not enough to simply assume a geometrically periodic microstructural distribution. In a valid RUC, periodicity is ensured by the application of periodic boundary conditions (PBCs), with general forms given in Equations 14-15 [**9**].

$$u_i^j(x+d) - u_i^j(x) = \bar{\varepsilon}_{ik} d_k^j \qquad \text{Eq. (14)}$$

$$\text{where } x \in \Sigma$$

$$T_i^j(x+d) - T_i^j(x) = 0 \qquad \text{Eq. (15)}$$

In these general forms, the average strain components over the RUC (and thus, the entire array) are represented by $\bar{\varepsilon}_{ik}$, the surface traction components by T_i^j, and d_k^j represents the distance between corresponding points x and $x + d$ in the *k*-th coordinate direction, which lie on opposing faces of the boundary surface Σ in the *j*-th direction. For example, consider the distance in the *x*-direction between point A and its image on the next RUC (for example, point B) on the corresponding faces in the $j = 1$ faces as shown in Figure 9. This is given by Equation 16.

$$d_k^j = x_k^{j+} - x_k^{j-}$$
$$d_1^1 = x_1^{1+} - x_1^{1-}$$
$$d_1^1 = x_B - x_A = (x_A + \ell) - x_A \qquad \text{Eq. (16)}$$
$$d_1^1 = \ell$$

Similarly, the distance in the *y*-direction between point A and point B on the corresponding faces in the $j = 1$ faces is given by Equation 17.

$$d_k^j = x_k^{j+} - x_k^{j-}$$
$$d_2^1 = x_2^{1+} - x_2^{1-}$$
$$d_2^1 = y_B - y_A = (y_A + 0) - y_A \qquad \text{Eq. (17)}$$
$$d_2^1 = 0$$

The concept of a periodic boundary condition (PBC) is actually quite simple – essentially, PBCs require that the displacements at corresponding points on opposite sides of an RUC are related, or linked. This can be understood by considering the array of repeating unit cells – each RUC is identical, such that a point x_0 within any of the RUC has its image within every other RUC in the array, separated by a distance *d*. Therefore, corresponding nodes on opposing surfaces of the RUC displace in the same manner, plus whatever volumetric strain effects resulting from applied loads. In addition, the resulting boundary tractions at corresponding points on opposing faces are in equilibrium. Note that the traction BCs in a finite element analysis are usually not explicitly prescribed, since they are natural boundary conditions and are generally satisfied automatically as part of the FEA solution process [**12**]. In summary, PBCs ensure continuity and compatibility between adjacent RUC, such as shown in Figure 9.

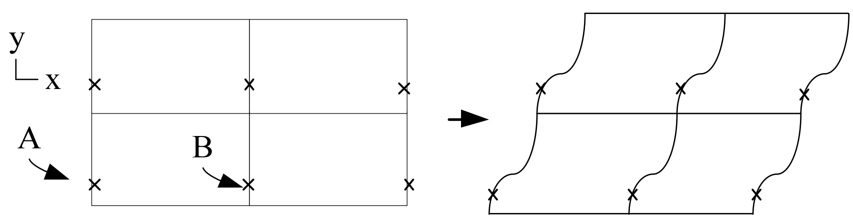

Figure 9. PBCs ensure that each RUC responds in an identical manner to loads, and the relative displacement of Point A and its image (represented by an "x" such as at Point B) on any other RUC are related by Equation 12.

In the RUC representation the inclusions are usually assumed to take hexagonal or rectangular arrangements, which are illustrated in Figure 10.

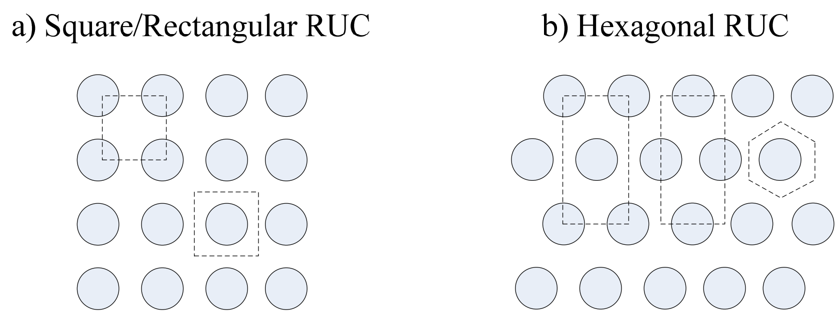

Figure 10. Typical RUCs for a) the square/rectangular, and b) the hexagonal periodic arrangements.

Although it is not a requirement, repeating unit cells often exhibit symmetry with respect to the *x*-, *y*-, or *z*-planes. In the case where reflective symmetry exists in terms of: 1) geometry, 2) support conditions, 3) material properties, and 4) mechanical loading, the solution obtained from the structural analysis will also be symmetric. Therefore, computational models need only represent the symmetric part of the RUC. This is obviously desirable in numerical calculations in order to further reduce computational requirements. For example, consider a fiber-reinforced composite material with a microstructure idealized as a square array of fibers as in Figure 11a.

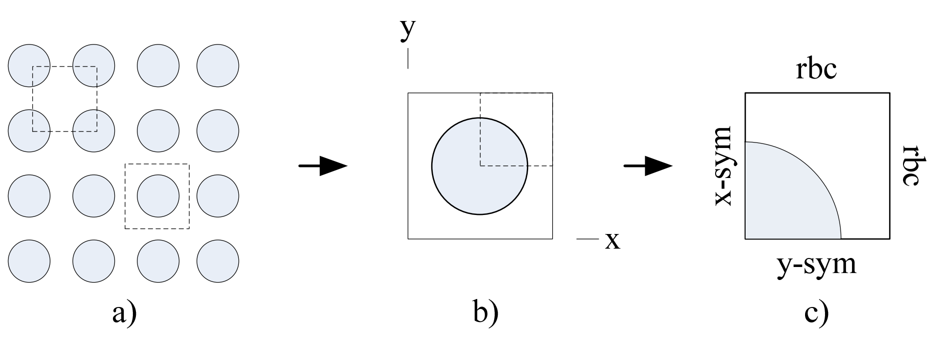

Figure 11. Derivation of the quarter-symmetric RUC. Mechanical loading is assumed to be in the fiber axial direction. Note that either of the RUCs indicated by the dashed lines on the left may be represented by the quarter-symmetric RUC on the right.

In this case the smallest valid repeating unit cell is a single fiber within a small region of surrounding matrix material, as shown in Figure 11b. In general terms, the application of PBCs to this geometry is sufficient for any load case. Now, supposing the applied loads act along the fiber axis only, the reflectional symmetries about the *x*- and *y*-planes may be exploited. Therefore, solutions obtained over a quarter-symmetric model as in Figure 11c fully describe the response of the entire RUC. Such reductions in the required model size allow an RUC to become much less computationally expensive, especially with respect to that of the RVE.

Arguably, the simplification of a composite microstructure as an idealized, regular, and periodic array of identical repeating unit cells is not always reasonable. Then again, the computational expense of an RVE may be prohibitive and the homogeneous displacement BCs (often referred to as the plane-remains-plane BC) may enforce artificial rigidity along boundary surfaces. Therefore, an awareness of the actual microstructural detail is required when attempting to model the behavior of a specific composite material.

Shear-Lag Stress Transfer

FRP composites are optimally designed to carry loads in the fiber direction, as shown in Figure 12. When loaded in such a manner (within the elastic limit and assuming that the fiber-matrix interface is perfectly bonded) the strains in the matrix and fiber are equal. In this ideal case, no shear stress exists at the interfacial boundary.

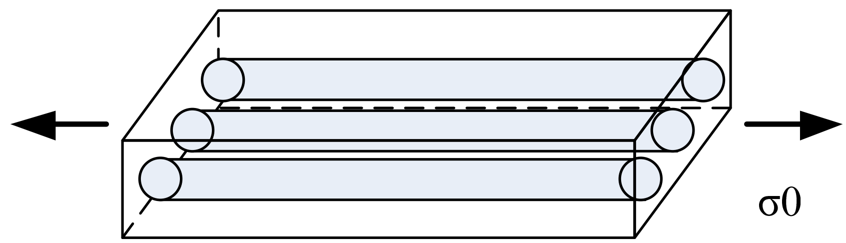

Figure 12. Loading of an FRP in the fiber axial direction.

However, at fiber breaks, fiber ends, or where the fiber-matrix interface is imperfectly bonded, the softer matrix material temporarily carries a greater portion of the load – consequently, a strain gradient exists across the interfacial boundary until the load is redistributed from the matrix to the broken fiber (and surrounding fibers) via intact fiber-matrix interfaces. This occurs through shear stresses at the fiber-matrix boundaries.

The analysis of stress transfer between fiber and matrix materials in composites is accomplished using a method commonly referred to as "shear-lag" analysis, originally proposed by Cox [**16**] and greatly expanded by Nairn [**17**] and others. Shear-lag models are usually represented by a single "broken" fiber embedded within a matrix material. Typically the fiber and matrix are arranged in concentric cylinders like the CCA, as illustrated in Figure 13a, although in some cases [**18**] other neighboring intact fibers are present.

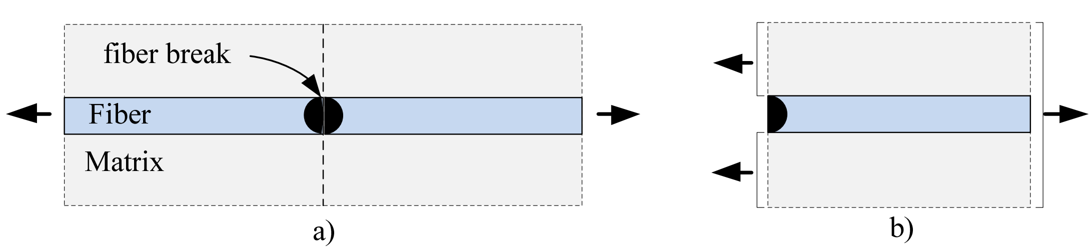

Figure 13. a) Shear-Lag conceptual model; b) Typical computational shear-lag model exploiting symmetry.

In this configuration, symmetry exists in the fiber axial direction about the fiber break; consequently, only half of the model is necessary as in Figure 13b. In order to simulate the broken fiber in the symmetric model, the fiber end is a free (unloaded) surface, while mechanical or displacement boundary conditions are normally applied to the matrix material only, which are then transferred from the matrix to the fiber through shear stresses that develop at the fiber-matrix interface.

Ineffective Fiber Length

Experimental results [**3**,**4**] have shown that until the maximum fiber tensile stress (σ) is recovered by a broken fiber, the nominal axial load is transferred from the matrix to the fiber through interfacial shear stress (τ) at the fiber-matrix boundary. For instance, in Figure 14 the photoelastic image of a single broken glass fiber in an epoxy matrix under tensile loading is shown [**4**], and the isochromatic fringes can be observed. In the photoelastic technique, the isochromatic fringes represent regions along which the difference between the principal stresses is constant, and are directly related to the shear stress. Therefore, the stress distribution at the fiber-matrix interface can be obtained from photoelasticity, such as indicated in Figure 15 [**19**].

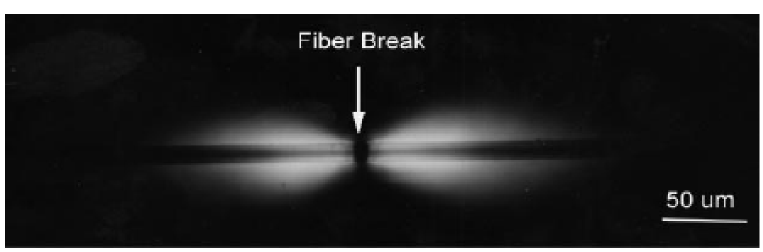

Figure 14. Photoelastic image of single fiber fragmentation test (E-glass/epoxy); the isochromatic fringe seen can be used to obtain the shear stress at the fiber-matrix interface [**4**].

The load transfer from matrix to fiber occurs over a finite length, as illustrated in Figure 16. On the left where the fiber break is represented, the shear stress at the fiber-matrix interface (τ_{int}) quickly increases to its maximum value. At the break, the fiber itself carries no load; thus, the axial stress within the fiber (σ_f) is zero and the entire axial load is borne in the matrix alone. As the load is transferred across the fiber-matrix interface through shear stress, the stiffer fiber carries a greater portion of the load and the strain mismatch between fiber and matrix gradually decreases. Simultaneously, σ_f increases from zero to the fiber's maximum load carrying capacity (σ_{max}) and τ_{int} decreases to zero. The length required for a broken fiber to recover a majority of the maximum load carrying capacity (typically, 50% or 90% of σ_{max}) is often referred to as the ineffective fiber length, or $\ell_{0.9}$.

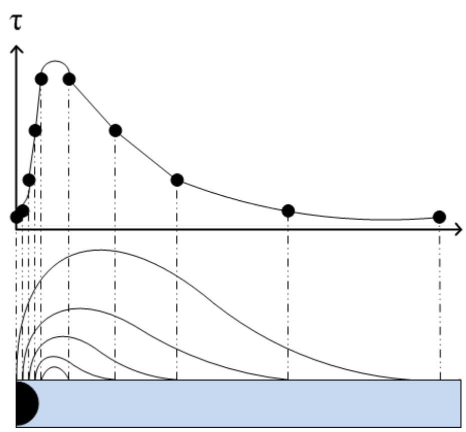

Figure 15. Example of the determination of shear stress at fiber-matrix interface from photoelasticity [**19**].

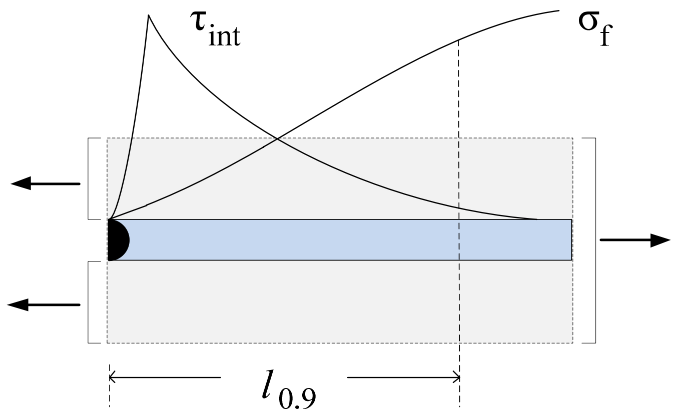

Figure 16. Lateral view of axial fiber stress (σ_f) and fiber-matrix interfacial shear stress (τ_{int}) distributions near a fiber break. The ineffective fiber length ($\ell_{0.9}$) is the fiber length required before 90% of the fiber load carrying capacity is recovered.

It is well documented in the literature that the fiber length required before σ_{max} is recovered is a function of fiber volume fraction (V_f) and the fiber-to-matrix modulus ratio (E_f/E_m). For example, as reported by Nairn [**17**] and Hossain et al. [**20**,**21**], $\ell_{0.9}$ decreases V_f increases, and increases as E_f/E_m increases.

Within the context of the current work, it is convenient to define a nondimensional form of the ineffective fiber length given by

$$\hat{L}_{inef} = \ell_{0.9}/D \qquad \text{Eq. (18)}$$

where:

$\ell_{0.9}$ = the 90% stress transfer distance (μm)

D = fiber diameter (μm)

This equation can be interpreted as the number of fiber diameters required before 90% of the maximum axial load has been recovered by a broken fiber.

Note that in linear elastic models, the ineffective fiber length does not change as load magnitude increases or decreases. Consider, for example, a repeating unit cell as shown in Figure 17, which represents a fiber-reinforced composite material where fibers are placed in a periodic square arrangement. Let $V_f = 0.30$, $D = 14$ μm, and $E_f / E_m = 20$. Surface loads at the positive *z*-face are placed on the matrix material only, in the fiber axial direction, in a manner consistent with the Shear-Lag method. The *xy*-plane is constrained in the *z*-direction only, and all other surfaces have appropriate PBCs.

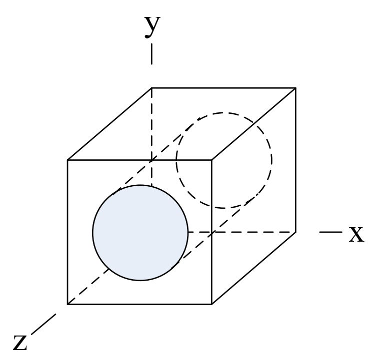

Figure 17. RUC for Shear-Lag FEA.

The axial stress distribution (σ_f) obtained from FEA along the length of the fiber is shown in Figure 18 for two boundary displacements in the *z*-direction:

1. $u_3 = 0.2$ μm
2. $u_3 = 0.4$ μm

Assuming a length of 35 μm in the *z*-direction, the nominal applied strain is approximately $\varepsilon_{33}^{0} = 0.57\%$ and $\varepsilon_{33}^{0} = 1.14\%$ for load case (1) and (2), respectively. The length of fiber required before 90% of the maximum stress developed within in each fiber is the same in each load case, as illustrated by the dotted lines in Figure 18. Of course, each model in this example has the same fiber diameter; therefore $\hat{L}_{inef}$ is the same in each model as well. The rate at which the axial stress within the fiber increases to its maximum is also the same, as shown in Figure 19. Thus, $\ell_{0.9}$ is a characteristic value for a given V_f and modulus ratio, and for linear elastic models does not change with load magnitude.

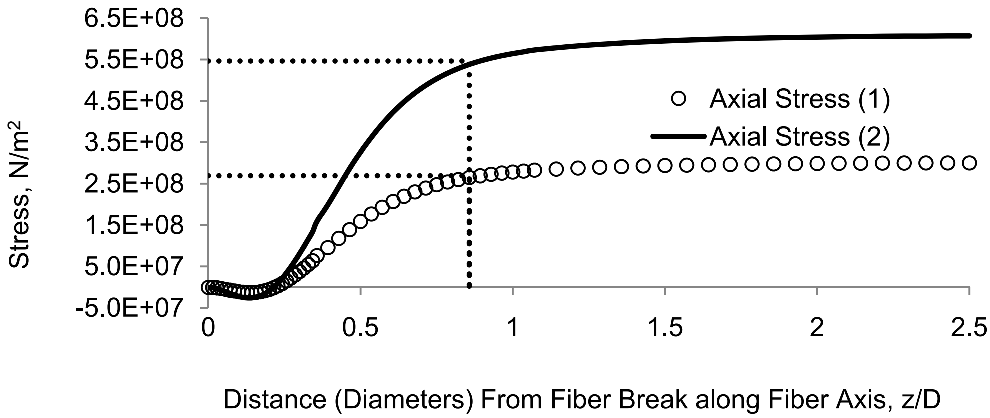

Figure 18. Ineffective fiber length for the single fiber RUC as a function of fiber diameter in two load cases. For $V_f = 0.30$, the 90% load transfer length is approximately 12.5 µm (or approximately 89% of a fiber diameter) for both load case (1) and (2).

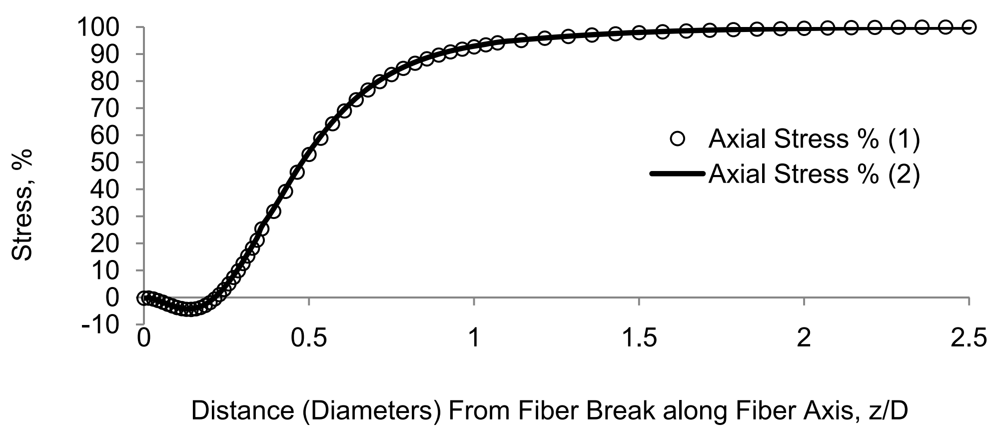

Figure 19. The percent of maximum axial stress for the single fiber RUC as a function of fiber diameter. The rate at which the maximum stress in each fiber is developed is the same for load cases (1) and (2).

Shear-lag models of various levels of complexity are found in the literature, ranging from the relatively simple linear elastic to those which incorporate material viscoelasticity, strain hardening, and damage parameters in an effort to reproduce experimental data. In most models, it appears that analytical shear-lag methods accurately predict fiber axial stresses [**17**], but have lower accuracy when predicting the shear stress at the fiber-matrix interface. To overcome this, detailed finite element models have been utilized [**18**,**22**,**23**]. However, very few results have been published regarding the effect of fiber diameter on the ineffective fiber length for a given fiber volume fraction. In fact, most analytical shear-lag models disregard this concept altogether. This is only just beginning to be recognized, as in the recent works of Hossain et al. [**21**] and Peterson et al. [**24**].

Damage and Fracture

An essential part of engineering design is to determine the ability of a structure to sustain design loads without incurring damage, as well as the ability to continue service in the presence of damage. Predicting the onset of damage and the potential for its subsequent growth is a challenging problem, as one might expect, and several failure theories are widely used in order to address the issue.

In general, damage mechanics and material failure models refer to the gradual loss of load-carrying capacity resulting from the degradation of the material stiffness, while fracture mechanics considers the growth of existing flaws. In this research, progressive damage and failure is simulated using the cohesive zone – a powerful and versatile method that, in many ways, combines the best aspects from both damage mechanics and fracture mechanics theories. The following sections give a brief overview of classical continuum failure theories and fracture mechanics in order to provide a general background, and to create a basis for comparison with the cohesive zone damage model.

Continuum Failure Theories

In certain classical failure theories, such as the Maximum Principal Stress (or Tresca) and Maximum Octahedral Shear Stress (or von Mises) Criteria, inelastic behavior is assumed to occur when a critical stress, strain, or strain energy has been reached. The failure criterion may be considered to be the resistance of a material to damage, however, effects from local defects on the microscale are not explicitly considered, and material behavior is taken on the macroscale only.

For example, at a material point where the applied load results in the three-dimensional principal normal stresses, σ_1, σ_2, and σ_3, the von Mises Criterion predicts that failure or yielding occurs when the effective stress (σ_{eff}) equals the material's critical stress (σ_c). Further loading results in permanent (plastic) deformation of the material. This criterion is given in Equation 19, in terms of the principal stresses.

$$\sigma_{eff} = \sigma_c = \frac{1}{\sqrt{2}}\sqrt{(\sigma_1 - \sigma_2)^2 + (\sigma_2 - \sigma_3)^2 + (\sigma_3 - \sigma_1)^2} \quad \text{Eq. (19)}$$

Classical failure theories implicitly assume the material to be homogeneous and free from large cracks or other geometric stress raisers. However, these types of geometric discontinuities are a common source of failure in engineering structures. As discussed by Dowling [**25**] and many other mechanics of materials texts, stress analyses for structural members with geometric discontinuities such as holes, fillets, blunt notches, or other stress raisers may be performed by determining an appropriate stress concentration factor,

$$k_t = \sigma/\sigma^0 \qquad \text{Eq. (20)}$$

which is the ratio of the maximum stress near a notch or crack (σ) to the nominal applied stress (σ^0). However, these methods are unable to accurately account for materials with sharp slit-like cracks, and where the crack tip radius tends to becomes small [**26**,**27**,**25**]. In fact, in such a case, σ becomes increasingly large near the crack tip – becoming theoretically infinite if the crack is ideally sharp.

Consequently, the field of continuum damage mechanics (CDM) has evolved in order to consider the initiation and growth of cracks at the microscale. In CDM a continuous damage variable (Φ) represents the overall material degradation over a process zone of finite size. Once a damage initiation criterion such as the von Mises effective stress above is satisfied, the overall damage variable increases according to a specified constitutive damage evolution law over the range $0 \le \Phi \le 1$. The stress field in the material is given by the general form in Equation 21 [**28**],

$$\boldsymbol{\sigma} = (1 - \Phi)\bar{\boldsymbol{\sigma}} \qquad \text{Eq. (21)}$$

where $\bar{\boldsymbol{\sigma}}$ is the stress field in the absence of damage. The material has lost its load carrying capacity when $\Phi = 1$. In finite element analysis, when the damage variable reaches maximum degradation, or when $\Phi = 1$, the element is typically inactivated and removed from the mesh [**29**]. Although a significant improvement over classical failure criterion alone, CDM does not generally allow the observation of discrete damage processes that are of interest in the current work, particularly regarding interfacial debonding.

Fracture Mechanics

Fracture mechanics addresses the problem of the integrity and durability of materials containing cracks or crack-like defects [**26**] using the concepts of strain energy and stress intensity. The concept of a critical energy threshold required to form new surfaces by crack extension is often traced back to the seminal work of Griffith [**30**].

In fracture mechanics, the stress intensities K_I, K_{II}, and K_{III} characterize the magnitude of the stresses near a crack tip in the Mode I, II, and II crack opening displacements, respectively. For example, in the opening mode of fracture (Mode I) the stresses near the crack tip are of the form given by the general form in Equation 22.

$$\sigma_{ij}^{I} = \frac{K_I}{\sqrt{2\,\pi\,r}}\, f_{ij}^{I}(\theta) + \cdots \qquad \text{Eq. (22)}$$

where:

r = the distance from the crack tip

θ = angle of rotation about the crack plane

K_I = the Mode I (opening) stress intensity factor

f_{ij}^{I} = defines the angular variation of the stress in Mode I

… = indicates the presence of higher-order terms in a series solution

For convenience the stress intensity factor, K_I, is often expressed as shown in Equation 23.

$$K_I = F \cdot \sigma\sqrt{a} \qquad \text{Eq. (23)}$$

Therefore, K_I relates the applied nominal stress (σ) and the crack size (*a*), where *F* is a dimensionless function of the crack size and placement as well as the overall specimen geometry [**25**], and can be found in most engineering handbooks. Thus, for a particular load and crack geometry a specific stress intensity factor K_I may be calculated, which characterizes the magnitude of the local stress field ahead of a crack. For example, in the classic example of an elliptical crack in a wide plate loaded in tension, as shown in Figure 20, the stress intensity K_I is

$$K_I = \sigma\sqrt{\pi\, a} \qquad \text{Eq. (24)}$$

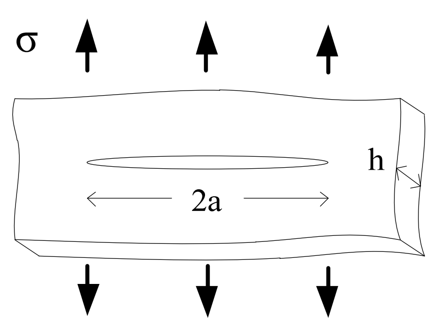

Figure 20. Infinite plate with an elliptical through-crack under tension.

In this method, an existing crack extends when the local stress intensity at a crack tip becomes critical; K_I at this point is known as the fracture toughness of the material,

K_c. Thus, in Mode I, failure is predicted when $K_I > K_{Ic}$. For the load case shown in Figure 20, the fracture toughness at the critical load is given by Equation 25.

$$K_{Ic} = \sigma_c \sqrt{\pi\, a} \qquad \text{Eq. (25)}$$

In fracture mechanics theory, when a material is loaded such that the stress state at the crack becomes critical, the crack extends by a small amount *da*. If the displacement at this critical point is held constant, then the stiffness of the member decreases. This results in a decrease in the potential energy in the member by *–dU*, and it is said that energy has been released by the formation of the new crack surface. The change in crack area is *h·da*, where *h* is the thickness of the member. The energy per unit crack area required to extend the crack is known as the critical strain energy release rate (*G*), and is given by

$$G = -\frac{1}{h}\left(\frac{dU}{da}\right) \qquad \text{Eq. (26)}$$

The strain energy release rate, originally conceived by Griffith, is considered to be the fundamental physical quantity controlling the behavior of the crack [**25**,**30**], and is generally taken to be a material property. It can be shown that the stress intensity (*K*) is related to the strain energy release rate (*G*) [**25**,**26**]. For mode I crack opening, the relation is given by Equation 27.

$$G = \frac{K^2}{E'} \qquad \text{Eq. (27)}$$

where

$$E' = E \text{ for plane stress; } \sigma_z = 0$$

$$E' = \frac{E}{1-\nu^2} \text{ for plane strain; } \varepsilon_z = 0 \qquad \text{Eq. (28)}$$

As seen in Equation 22 above, the stresses at the crack tip approach infinity as *r* approaches zero (nearing the crack tip). Thus, the crack tip in LEFM is known as a singular point, and no realistic value of stress can be obtained. Also, in defining *K*, the material is assumed to behave in a linear elastic manner [**25**], therefore this approach is called linear elastic fracture mechanics (LEFM). LEFM successfully describes fracture in isotropic and relatively brittle materials, where the fracture process zone at the crack tip is small and there is little or no plastic (nonlinear) deformation [**25**,**27**]. In most real materials, however, a redistribution of stresses occurs at the crack tip due to plasticity, crazing, or microcracking [**25**,**27**,**31**]. In each case, the crack tip develops a finite separation near its tip – thus, the very high stresses predicted by both concentration factors and by LEFM are redistributed within the region surrounding the crack tip. In addition, for LEFM to be practically applied an initial crack must exist in the material. Therefore, fracture mechanics cannot be applied to predict the nucleation, or initiation, of voids or microcracks within a material to form a new crack.

Overview of the Cohesive Zone Model

In the cohesive zone model (CZM), damage and fracture is viewed as a phenomenon that takes place across an extended zone in front of a crack tip, in which the growth of the crack is resisted by internal cohesive forces [**32**]. Within this cohesive process zone, the effects of all mechanisms of irreversible material degradation (such as shown in Figure 21) are lumped together [**33**]. First introduced by Dugdale [**32**] and Barenblatt [**34**], CZMs have been successfully used to model a number of fracture and failure processes, most notably in the analysis of adhesive joints and interfacial delamination in composites.

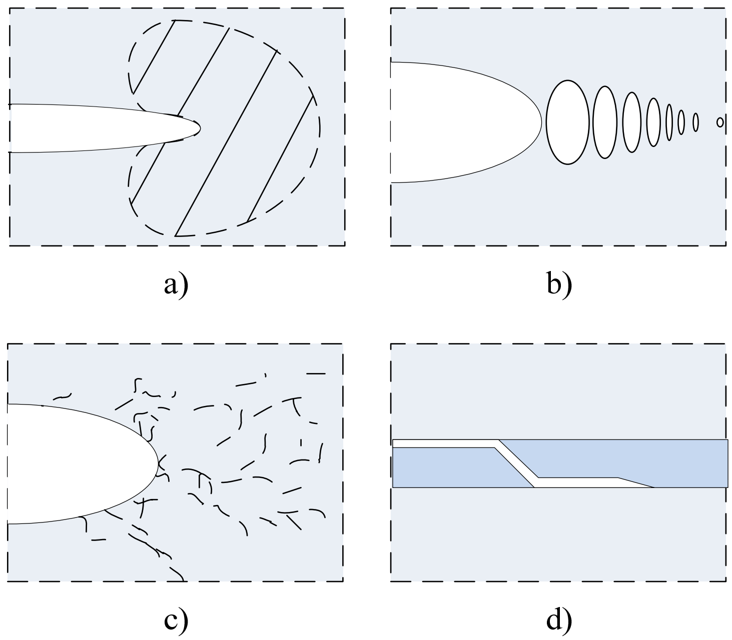

Figure 21. In real materials, nonzero radii are often accompanied by stress redistribution due to a) plasticity, b) crazing, c) microcracking, or d) delamination.

In debonding and decohesion failure where the initial separation between debonding surfaces is negligibly thin, damage mechanisms present within an element may be represented using a traction-separation (T-δ) relation. In this case, cohesive elements are placed in the mesh between surrounding continuum elements, forming an "interface" in which damage may occur and the surrounding continuum elements may separate, as shown in Figure 22.

In the CZM, once a damage initiation criterion is met, material (interfacial) damage may occur according to a specified damage evolution law. Thus, the CZM is influenced by the surrounding bulk material properties, the crack initiation condition, and the crack evolution function [**35**].

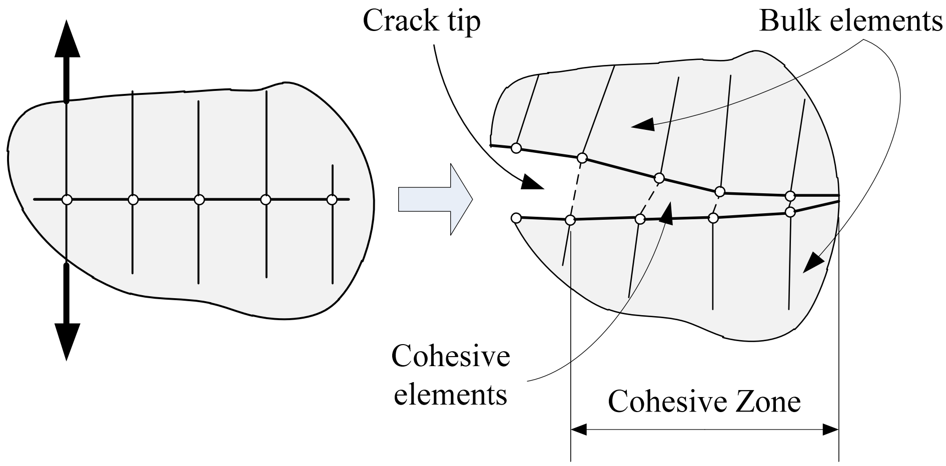

Figure 22. Interfacial cohesive elements before and after separation. Irreversible damage occurs in the cohesive zone; the crack tip is permitted to extend when an element is fully degraded.

To further understand these concepts, consider the general framework of damage mechanics. This framework consists of four parts, and can be demonstrated using the simple CZM bilinear traction-separation relation as defined in Figure 23.

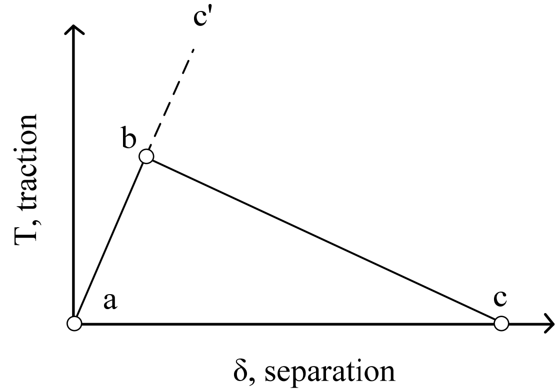

Figure 23. The CZM bilinear traction-separation relation.

These four parts are:

1. An initial, undamaged (linear elastic) constitutive behavior (path *a-b-c'*);
2. Damage initiation (point *b*), representing the interfacial strength;
3. Damage evolution (path *b-c*), representing the process of material degradation;
4. Choice of element deletion upon complete material degradation (point *c*).

In a related sense, the key material properties required to define the interfacial behavior of the bilinear CZM are:

1. The initial, undamaged elastic stiffness, K_0;
2. The interfacial cohesive strength, T_c;
3. The interfacial fracture energy, G_c.

The CZM method is particularly successful when the crack path is known *a priori*. In many simulations, knowledge of the most probable crack path is achieved through prior experimental observation. For example, in composite laminates a common mode of failure occurs through the delamination of individual plies – therefore, cohesive elements are often placed at the interfaces between the plies in order to capture the onset and spread of interlaminar damage. The cohesive zone model approach offers several advantages for modeling failure in composite materials, including:

1. The fracture process zone in quasi-brittle materials (such as composites) may be larger than allowed by LEFM;

2. Both the initiation and evolution of damage may be predicted without the need for a pre-existing crack, nor is the geometric shape of the crack tip required;
3. Material degradation, or a gradual loss of stiffness, may be associated with the damage evolution function;
4. Multiple damage initiation criterion and failure mechanisms may be simultaneously employed;
5. Crack growth may potentially occur along any path where cohesive elements have been placed.

Cohesive Element Formulation

In this research the built-in cohesive element formulation and traction-separation relation provided by the commercial finite element code Abaqus are used. The following section describes the cohesive element and traction-separation (T-δ) formulations, and their implementation in FEA damage models.

Element Geometry. The elements used for this study[§] take the form of three-dimensional 8-node (linear) solid hexahedrons with three displacement degrees of freedom (DOF) at each node, as shown in Figure 24.

[§] Abaqus element code: COH3D8

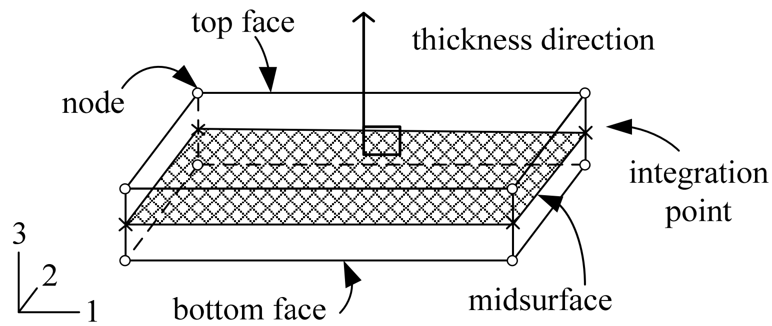

Figure 24. Key geometric features of a cohesive element.

As indicated in the figure, cohesive elements are associated with a thickness direction. Conceptually, cohesive elements can be considered as a pair of top and bottom faces, separated by a thickness [**29**]. The midsurface passes through the integration points of the element, which are defined by averaging the coordinates of the node pairs at the vertices of the top and bottom faces. The thickness direction is assumed to be normal to this midsurface. The relative motion of the top and bottom faces measured along the thickness direction represents opening or closing displacements of an interface.

Thickness and Material Parameters. The initial thickness (H_o) of the cohesive element may correspond to the geometric thickness that has been modeled using the mesh nodal positions and stack direction, or it may be specified directly. This is an important choice that affects the behavior of the element, and is particularly relevant in interfacial problems where the initial thickness may be very small or zero – in such a case, the thickness computed by nodal coordinates may not be accurate due to round-off errors [**29**] and direct specification should be used.

Material parameters used in the cohesive zone T-δ formulation can be thought to describe the mechanical behavior of an interface, rather than any real physical material.

The interpretation of material properties, such as the elastic stiffness, as interface parameters is interesting in the limit case as the thickness of a cohesive element tends to zero. Consider, for example, the axial displacement (δ) of a rod under a loading force (*F*) is

$$\delta = \frac{F}{k_{eq}} = \frac{FL}{AE} \qquad \text{Eq. (29)}$$

where k_{eq} is the equivalent stiffness of the rod, *A* is the cross-sectional area of the rod, *E* is the modulus of elasticity, and *L* is the rod length. As an analogue to the elementary equation $\varepsilon = \sigma/E$, Equation 29 may be rewritten as $\delta = \sigma/K$ where the axial stress is $\sigma = F/A$ and the constitutive stiffness is $K = E/L$. As a matter of convenience, if the length L is now replaced by the unit value 1.0, then the strain is the same as the displacement.

$$\varepsilon = \delta \text{ if } L = 1 \qquad \text{Eq. (30)}$$

In the *T*-δ formulation, if an adhesive material has a modulus of E_c and an initial thickness H_0, then the interface stiffness is given by Equation 31, which relates the nominal stress across the interface to its displacement separation in the same manner as $K = E/L$.

$$K = E_c/H_0 \qquad \text{Eq. (31)}$$

However, it can be seen that for an interface with a negligibly small initial thickness, the stiffness *K* approaches infinity. In addition, both H_0 and *K* are difficult to physically measure, and are generally unknown. Along these lines, the cohesive element initial thickness may be manually defined as a unit value – regardless of the length scale or mesh coordinates used in the actual model. Consequently, the strains across the interface are the same as the relative displacements of the top and bottom surfaces of the cohesive element (as in Equation 30 above).

Connectivity. Cohesive elements are meant to represent an interface; they may not be layered in the thickness direction. Therefore, the cohesive zone may only be discretized using a single layer of cohesive elements through its thickness [**29**]. Cohesive elements may be joined to adjacent continuum (bulk) elements by sharing nodes, or with tie constraints (see Figure 25).

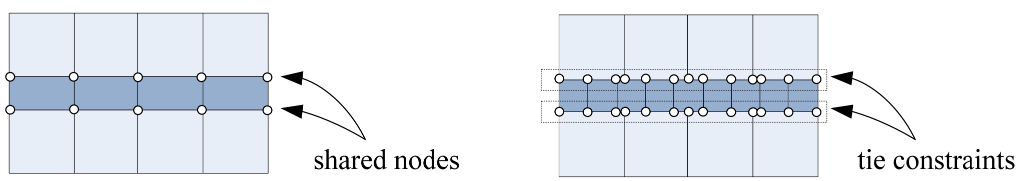

a) Node sharing:
A single meshed part is used. Cohesive elements are embedded in mesh next to surrounding bulk elements.

b) Tie constraints:
Three separate meshed parts are used. Cohesive elements in a finely discretized region are tied to surrounding bulk elements.

Figure 25. Cohesive element connectivity using a) node sharing, and b) tie constraints for mismatched meshes.

As illustrated in Figure 25a, node sharing is possible when the cohesive elements are the same size as the surrounding bulk elements. Generally, mesh creation using node sharing is easy to implement; however, more accurate results (and higher resolutions) are obtained when the cohesive zone is finely meshed. If both cohesive zone and bulk elements are finely meshed, the total number of elements in the mesh may become quite large and computationally expensive. To avoid this problem, the cohesive zone may be more finely discretized than the surrounding bulk elements with boundary connectivity enforced by tie constraints, as indicated in Figure 25b. An additional benefit of using tie constraints is that linear cohesive elements may then be joined to an adjacent mesh of higher-order quadratic elements used for the bulk material on either side of the interface.

Traction-Separation Relation. At an initially bonded interface, let the initial geometric distance between two surfaces be zero, or otherwise negligibly small. Accordingly, the top and bottom surfaces of a cohesive element are collapsed upon themselves, as shown in Figure 26. As a result, the nodes from the top and bottom surfaces are superimposed, but retain independent DOF. In this configuration, the element thickness is equal to zero, and the constitutive response of a cohesive element is described using the traction-separation relation.

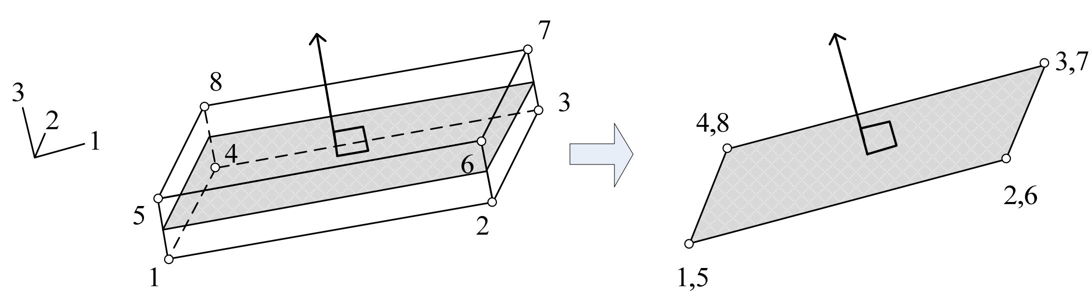

Figure 26. Collapsed cohesive element geometry at a bonded interface.

The T-δ relation assumes initially elastic behavior as the top and bottom surfaces begin to separate under loading, followed by damage initiation and evolution until complete material degradation is assumed to occur. When the cohesive element fails it is removed from the mesh, and the surrounding bulk elements are no longer bonded. This failure process is assumed to capture all mechanisms of damage, such as the nucleation, growth, and coalescence of voids and the growth of cracks.

The shape of the *T*-δ relation varies in the literature. For instance, the exponential type of Needleman [**36**] is shown in Figure 27a, the trapezoidal type of Tvergaard and Hutchinson [**37**] in Figure 27b, and the bilinear type of Camanho and Davila [**38**] in Figure 27c. However, each curve has in common certain essential features, namely:

1. An initial, undamaged (linear elastic) constitutive behavior;
2. Damage initiation, representing the interfacial cohesive strength;
3. Damage evolution, representing the process of material degradation;
4. Choice of element deletion upon complete material degradation.

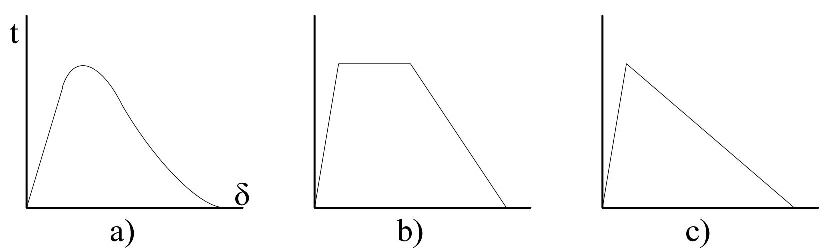

Figure 27. Common variations in the shape of the *T*-δ relation.

Cohesive Strength and Fracture Energy. The CZM is characterized in large part by both the critical stress criterion and the critical fracture energy. Like CDM, a critical stress criterion specifies the onset of damage. However, the evolution of the damage variable and the essential criterion for ultimate failure and damage progression is a function of the critical fracture energy, as in fracture mechanics. This flexible twoparameter approach allows cohesive zone models to predict fracture and failure in many types of materials and damage processes.

Penalty Stiffness. When traction-separation cohesive behavior is used, a high initial stiffness (K_0) is chosen in order to prevent deformation across the interface while loading occurs in the linear elastic pre-damage regime. Notice that the value of K_0 may be obtained from the shape of the bilinear traction-separation curve, as in Equation 32, where T_c is the cohesive strength damage initiation criterion and δ_c is the critical displacement at the onset of damage. Notice that the onset of damage may be fully defined by either the critical cohesive strength (T_c) or by the critical displacement (δ_c); however, K_0 automatically defines whichever value has not already been specified by using Equation 32.

$$K_0 = T_c/\delta_c \qquad \text{Eq. (32)}$$

After the interfacial tractions attain the cohesive strength, the damage initiation criterion (T_c) is satisfied. Subsequent irreversible reduction in stiffness occurs, and the stiffness may then be described as

$$K_\Phi = (1 - \Phi)K_0 \qquad \text{Eq. (33)}$$

where K_Φ is used to indicate the initial stiffness before a reduction due to damage. Before complete failure occurs, upon unloading the traction across the interface elastically reduces to zero over a path described by K_Φ, as shown in Figure 28. Upon reloading, the tractions across the interface elastically increase until the maximum value that the damaged element may carry has been recovered (defined here as the residual cohesive strength). Complete degradation of the element occurs when the fracture energy (G_c) has been satisfied, which is the area under the T-δ curve. Once complete degradation has occurred, $K_\Phi \rightarrow 0$ and the element can no longer resist further deformation. In this work, the element is removed from the mesh (deleted) when the damage variable equals one, or $\Phi = 1$, and the crack tip extends.

As an aside, although it has not been exploited in this research, it is noted that the irreversible damage process in stiffness and the corresponding residual cohesive strength may be useful in simulations of progressive damage in fatigue.

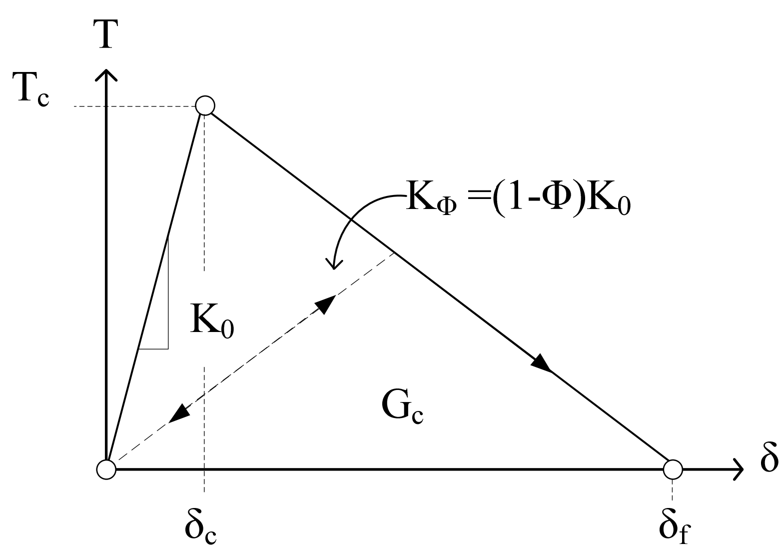

Figure 28. Bilinear traction-separation relation.

Nominal Stresses and Strains. The nominal stresses in a cohesive element, **T**, are the force components divided by the original area at each cohesive element integration point. The nominal strains, **ε**, are the separations between the top and bottom surfaces divided by the original thickness at each integration point. The nominal stresses are related to the nominal strains by an elastic stiffness matrix, ***K***, as in Equation 34, where the three component directions *n*, *s*, and *t* represent the normal (along the local 3-axis in the thickness direction) and the shear and transverse shear directions (along the local 1- and 2-directions).

$$\boldsymbol{T} = \begin{Bmatrix} T_n \\ T_s \\ T_t \end{Bmatrix} = \begin{bmatrix} K_{nn} & K_{ns} & K_{nt} \\ K_{ns} & K_{ss} & K_{st} \\ K_{nt} & K_{st} & K_{tt} \end{bmatrix} \begin{Bmatrix} \varepsilon_n \\ \varepsilon_s \\ \varepsilon_t \end{Bmatrix} = \boldsymbol{K\varepsilon} \qquad \text{Eq. (34)}$$

Using the original thickness H_o, the nominal strains are given by Equation 35.

$$\boldsymbol{\varepsilon} = \begin{Bmatrix} \varepsilon_n \\ \varepsilon_s \\ \varepsilon_t \end{Bmatrix} = \frac{1}{H_o} \begin{Bmatrix} \delta_n \\ \delta_s \\ \delta_t \end{Bmatrix} \qquad \text{Eq. (35)}$$

Recall, by defining the initial thickness $H_0 = 1$, the strains $\boldsymbol{\varepsilon}$ are the same as the displacements across the cohesive element, δ_i. In light of the previous discussions regarding the damage variable, constitutive thickness, and penalty stiffness, the bilinear traction-separation relation may be concisely given by Equation 36-39 [**29**,**38**].

$$t_i = \begin{cases} K_0 \delta_i & \text{for } \delta_i^{max} \leq \delta_i^c \\ (1 - \Phi) K_0 \delta_i & \text{for } \delta_i^c \leq \delta_i^{max} \leq \delta_i^f \\ 0 & \text{for } \delta_i^{max} \geq \delta_i^f \end{cases} \qquad \text{Eq. (36)}$$

with

$$\Phi = \frac{\delta_m^f (\delta_m^{max} - \delta_m^c)}{\delta_m^{max} \left(\delta_m{}^f - \delta_m^c \right)} \qquad \text{Eq. (37)}$$

where

$$\delta_m = \sqrt{\langle \delta_n \rangle^2 + \delta_s^2 + \delta_t^2} \qquad \text{Eq. (38)}$$

and

$$\delta_m^f = 2\, G_c / T_c \qquad \text{Eq. (39)}$$

where:

δ_m = the effective displacement across the element surfaces

δ_m^c = the critical effective displacement at damage initiation

δ_m^f = the critical effective displacement at complete material degradation

δ_m^{max} = the maximum effective displacement achieved during loading

MODEL DEVELOPMENT

Conceptual Model

In the fiber-scaling method discussed in previous sections, the fiber-matrix interfacial surface area may be increased by using more fibers. However, for a specified volume, the fiber volume fraction may remain constant if the fiber diameter is reduced while the number of fibers increases – consequently, the total mass of the composite material remains unchanged even as the fiber-matrix surface area increases.

In this work, the primary goal is to investigate the effect that fiber diameter and the total fiber-matrix interfacial surface area have upon the mechanical properties of a composite material. In order to accomplish this task the model itself need not be particularly complex. Models developed for the comparative analyses of this work are based upon appropriately simplified geometry. For example, consider the idealized cross-section of a typical glass-fiber reinforced epoxy lamina shown in Figure 29. In this idealization, fibers are assumed to be continuous, regularly spaced, and cylindrical in shape. The lamina is assumed to extend indefinitely in the *xz*-plane.

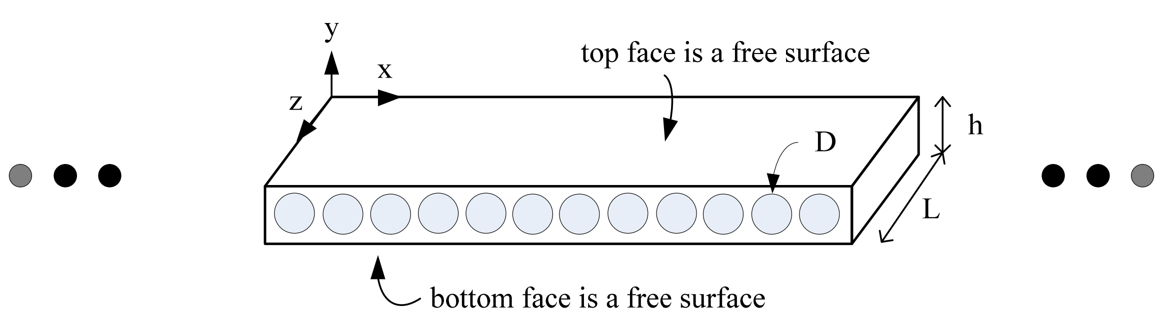

Figure 29. Idealization of an FRP composite lamina. This simplified geometry forms the basis for model development in the current work.

The conceptual geometry shown in Figure 29 forms the basis for model development in the current work. It is interesting to note that this simple configuration shares the essential details of many micromechanical models commonly found in the literature, with one important difference: the presence of free boundary surfaces on the top and bottom of the lamina. Unlike the RVE and RUC micromechanical representations, the conceptual structural geometry in Figure 29 does not assume that the model represents a material point within a much larger body. In fact, the opposite is true – the present model represents a structural volume within a very thin body, such that the diameters of the fiber reinforcements are on the same order as the thickness of the lamina structure. This type of microstructural model is, strictly speaking, not a valid RVE for this very reason. However, it does not appear to violate any specific requirements of the RUC. If one likes, the conceptual geometry used in this work may be considered to be a special case of RUC, in which repeating boundary conditions (RBCs) are used in order to replicate a smaller subvolume within the plane of the structure only, rather than the usual periodic boundary conditions (PBCs) applied to all surfaces.

It is also worthwhile to mention that typical micromechanical models using the RVE or RUC representations do not strictly require the size of the inclusions to be known. Provided the fiber volume fraction V_f is maintained, the RVE and RUC may assume any dimensions. This is implicitly recognized by unit cell methods, in which a volume with unit lengths may be used for analysis, and the inclusion dimensions are governed by the V_f requirements.

Consider the following as an example: as shown in Figure 30a, suppose a material represented by RUC-1 has fibers of diameter $D_1 = 20$ µm, a width of $h = 40$ µm, and a length of $L = 200$ µm. The fiber volume fraction is therefore $V_f = 0.196$.

Now, as shown in Figure 30b, RUC-2 represents a similar material with the same fiber volume fraction as RUC-1, but with $D_2 \leq D_1$ such that in order to have the same V_f as RUC-1, the number of fibers, N_f, must increase to 9. The fiber diameter in RUC-2 may be calculated in order to yield $D_2 = 6.67$ µm.

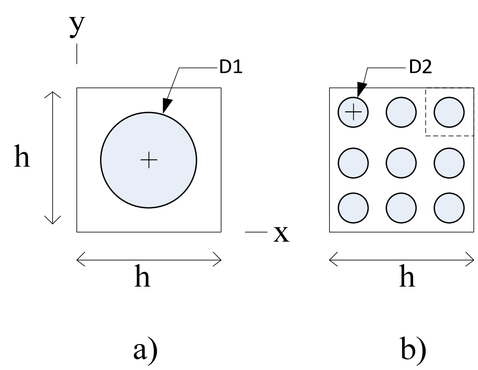

Figure 30. RUC models with equal V_f.

However, the differences in fiber diameters and outside width dimensions is obscures the fundamental relationship between the ratio of fiber diameter to the overall volume (that is, the fiber volume fraction, V_f). In fact, these two models are mathematically identical and cannot be used to demonstrate differences in fiber diameter and total interfacial surface area effects, as is the objective of this research. For the same reaction force generated by a given load condition, they will each respond in an identical manner.

This similarity can be demonstrated in a simple example: consider the fiber volume fractions resulting from each unit cell,

$$V_{f1} = \frac{\frac{\pi}{4}D^2L}{h^2L} = V_{f2} = \frac{N_f\frac{\pi}{4}D^2L}{h^2L} = 0.196 \qquad \text{Eq. (40)}$$

But, the same fiber volume fraction will also result from considering only one of the subvolumes about a single fiber within RUC-2 as indicated by the dashed lines in Figure 30b, as demonstrated in Equation 41.

$$V_{f2,sub} = \frac{\frac{\pi}{4}D^2L}{(h/3)^2L} = V_{f2} = \frac{N_f\frac{\pi}{4}D^2L}{h^2L} = 0.196 \qquad \text{Eq. (41)}$$

Thus, each model is the same by the nature of the geometric ratio *D*/*h*, the periodic replication of inclusions, and the imposed repeating boundary conditions. Moreover, from the calculations above, it should be expected that any length is sufficient, as long as the stress field is allowed to fully develop along the length of the RUC.

Therefore, the choice to include free boundary surfaces in the structural unit cell is twofold. The primary reason, as described above, is that RUCs based on fiber volume fractions alone cannot represent differences in fiber diameters, or account for an increase in fiber-matrix interfacial surface area.

Secondly, this allows the investigation into potential fiber-scaling benefits for fiber-reinforced membrane-like materials such as used in gossamer spacecraft. For example, the durability, performance, and longevity of gossamer spacecraft may be enhanced through the use of fiber reinforcements, while maintaining relatively low mass and compact stowage characteristics. Provided an increase in durability results from fiber-scaling for the same overall mass, reducing the fiber diameter could provide exceptional advantages. In addition, given that the thickness of many gossamer membranes may be considerably less than conventional fiber diameters, going to smaller diameter fibers may be the only practical solution.

Structural RUC Models

The key premise to this work is that the number of fibers and the total fiber-matrix interfacial surface area increases as the fiber diameter is reduced, provided the fiber volume fraction remains constant within a well-defined volume. The structural repeating unit cell model, or structural RUC, outlined in the previous section forms the basis for the development and investigation of this concept. Note that in each model, the fiber volume fraction is maintained at

$$V_f = 0.32$$

General Boundary Conditions

In the following sections, three models are presented which will be used in further analyses to represent the thin FRP lamina structure, and will enable the investigation into fiber-scaling effects. In each case, a fiber volume fraction of 32% is ensured by adjusting the fiber diameter and the number of fibers as required, within a well-defined volume using the fiber-scaling method. The volume for each structural RUC is defined by the height, width, and length:

$$h = w = 25\ \mu m$$
$$L = 160\ \mu m$$

The boundary conditions placed on each model are exactly the same. In fact, each model may be thought of as a variation of the same structural RUC, for each fiber diameter considered. In this sense, the combination of the two fundamental concepts employed in this research (namely, the fiber-scaling method and the structural RUC) may be considered as a technique to allow analyses upon the same structure using a different "material". Because each model represents the same structural component, the boundary conditions placed upon them may be discussed without special attention to the number and diameter of the fibers within them.

As such, the boundary conditions used in each analysis and for each model are illustrated in Figure 31. Boundary conditions on each of the six faces are indicated.

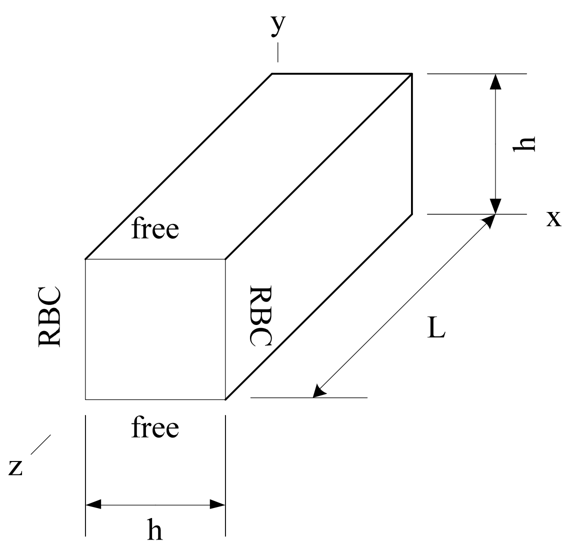

"Roller" condition applied to the -*z* face:
$u_3(x,y,0) = 0$

RBC on the ±*x* faces:
$u_1(h,y,z) = u_1(0,y,z) + h\cdot\varepsilon'_{11}$
$u_2(h,y,z) = u_2(0,y,z)$
$u_3(h,y,z) = u_3(0,y,z) + h\cdot\varepsilon'_{13}$

Loading applied to the +*z* face:
$u_3(x,y,L) = \Delta U3$

Free surfaces on the ±*y* faces:
$u_3(x,0,z) = u_3(x,0,z)$
$u_3(x,h,z) = u_3(x,h,z)$

Figure 31. General BCs used on structural RUC.

Loads are introduced on the +*z*-face in the fiber axial direction. The -*z*-face is constrained from movement in the *z*-direction only (and can be considered a symmetry plane). Importantly, the free boundary surfaces on the top and bottom faces of the structural RUC model must be included in the analyses, so that changes in the fiber diameter may be realized in the numerical solution – thus, the top and bottom surfaces are unloaded.

Repeating Boundary Conditions. Note that through the application of RBCs to corresponding points on the $+x$ and $-x$ faces, the structural RUC may be assumed to repeat infinitely in the horizontal direction. The specific form of the RBCs depend on the loading conditions, and are given in Equation 42 for a general case where repeating boundary conditions are placed on opposing faces in the x-direction. Notice that the relative displacements of corresponding points are specified as a function of the coordinates, and the surfaces are not required to remain a plane after loading and deformation.

$$\begin{aligned} u_1(h,y,z) &= u_1(0,y,z) + h\,\bar{\varepsilon}_{11} \\ u_2(h,y,z) &= u_2(0,y,z) \\ u_3(h,y,z) &= u_3(o,y,z) + h\,\bar{\varepsilon}_{13} \end{aligned} \qquad \text{Eq. (42)}$$

Further explanation of the RBC may be useful. Notice that, the RBC in Equation 42 introduces two extra DOF into the system: the average shear strain ($\bar{\varepsilon}_{13}$) and the average strain in the x-direction ($\bar{\varepsilon}_{11}$) [**12**]. These may be introduced in an FE analysis as independent degrees of freedom to the overall system; this may be accomplished by creating or choosing special nodes with one DOF (that is, where all but one DOF are constrained). Including these extra DOF in the RBC equations creates an average, or a "macroscopic," strain effect over the entire RUC. In addition, prescribed displacements or forces may be applied to these DOF in order to impose average strains or stresses over the system. Now, for symmetrical loads in the axial direction, no shearing stresses or strains exist, and $\bar{\varepsilon}_{13} = 0$. Therefore, only the average strain ($\bar{\varepsilon}_{11}$) remains. For axial loads, this DOF is left "free" so that the average stress is $\bar{\sigma}_{11} = 0$. The nodal displacement at this extra DOF gives the average strain directly [**12**], and relates the displacements between the corresponding points on the opposing *x*-faces directly produced by an axial load as a result of the Poisson effect.

Symmetry RBC. Notice, the RBC must be modified to account for the use of symmetry. For symmetry in the *x*-direction ("x-symm") the displacements at the plane of symmetry are given by Equation 43.

$$\begin{aligned} u_1 &= 0 \\ u_2 &= u_2 \rightarrow free \\ u_3 &= u_3 \rightarrow free \end{aligned} \qquad \text{Eq. (43)}$$

Symmetry conditions on the two opposing *x*-faces require

$$\begin{aligned} u_1(h, y, z) &= -u_1(0, y, z) \\ u_2(h, y, z) &= u_2(0, y, z) \\ u_3(h, y, z) &= u_3(0, y, z) \end{aligned} \qquad \text{Eq. (44)}$$

Therefore, the RBC relating the displacements of points on the +*x*-face in the symmetric model becomes

$$\begin{aligned} &u_1(h, y, z) = u_1(0, y, z) + h \cdot \bar{\varepsilon}_{11} \\ &\text{or} \\ &u_1(h, y, z) = h/2 \cdot \bar{\varepsilon}_{11} \end{aligned} \qquad \text{Eq. (45)}$$

Recall, the average strain $\bar{\varepsilon}_{11}$ in the *x*-direction is an "extra" DOF of the system. When a value is not directly prescribed, it serves only to relate the magnitude of the displacements in the *x*-direction for each node at the surface.

Model 1

Conceptually, the geometry associated with Model 1 (M1) is shown in Figure 32 where the fiber diameter is

$$D_1 = 16\ \mu m$$

Therefore, the length is equal to $10D_1$. The structural RUC derived from the conceptual geometry is shown in Figure 33a. Only one fiber is required in order to obtain $V_f = 0.32$. Utilizing symmetry about the x- and y-planes, the quarter-symmetric structural RUC indicated in Figure 33b is obtained for computational purposes.

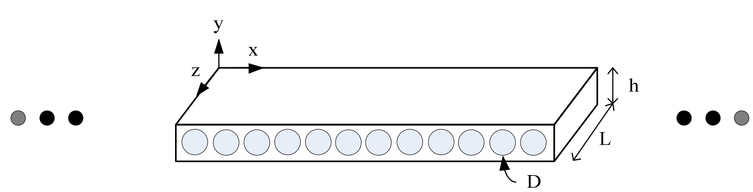

Figure 32. Model 1 conceptual geometry.

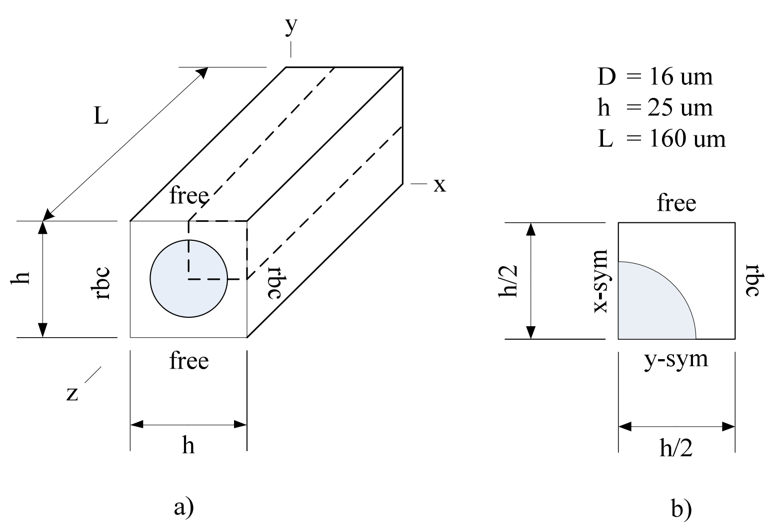

Figure 33. a) The M1 structural RUC; dashed lines indicate the location of the b) 1/4-symmetric structural RUC.

Model 2

Conceptually, the geometry associated with Model 2 (M2) is shown in Figure 34 where the fiber diameter is

$$D_2 = 8\ \mu m$$

Therefore, the length is equal to $20D_2$. Using Equation 5, it can be seen that because $D_2 = 1/2D_1$ four fibers are necessary in order to maintain the fiber volume fraction at 32%. The geometry and RBCs associated with Model 2 (M2) are shown in Figure 35a. Full exploitation of symmetry about the *x*- and *y*-planes results in the 1/8-symmetric structural RUC indicated in Figure 35b.

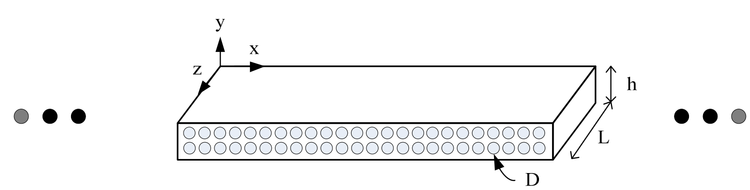

Figure 34. Model 2 conceptual geometry.

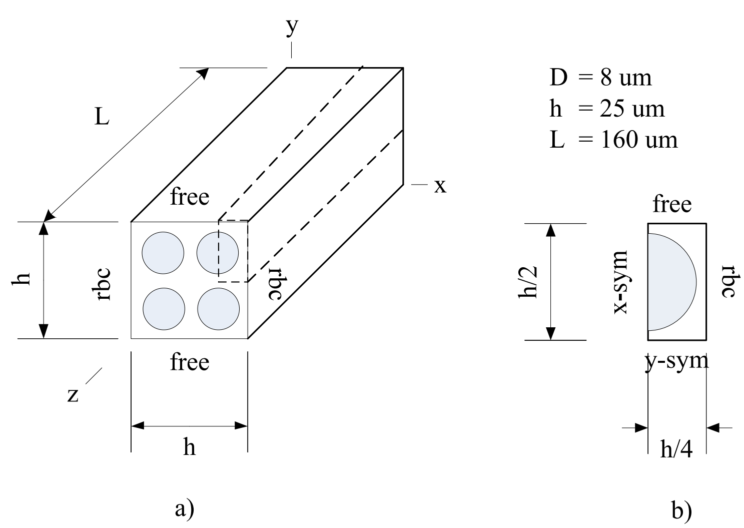

Figure 35. a) The M2 structural RUC; dashed lines indicate the location of the b) 1/8-symmetric structural RUC.

Model 3

Conceptually, the geometry associated with Model 3 (M3) is shown in Figure 36 where the fiber diameter is

$$D_3 = 4\ \mu m$$

Therefore, the length is equal to $40D_3$. The structural RUC derived from the conceptual geometry is shown in Figure 37a. Using Equation 5, it can be seen that because $D_3 = 1/4D_1$ sixteen fibers are necessary in order to maintain the fiber volume fraction at 32%. Full exploitation of symmetry about the *x*- and *y*-planes results in the 1/16-symmetric structural RUC indicated in Figure 37b.

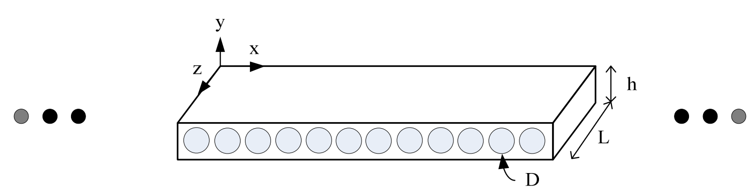

Figure 36. Model 1 conceptual geometry.

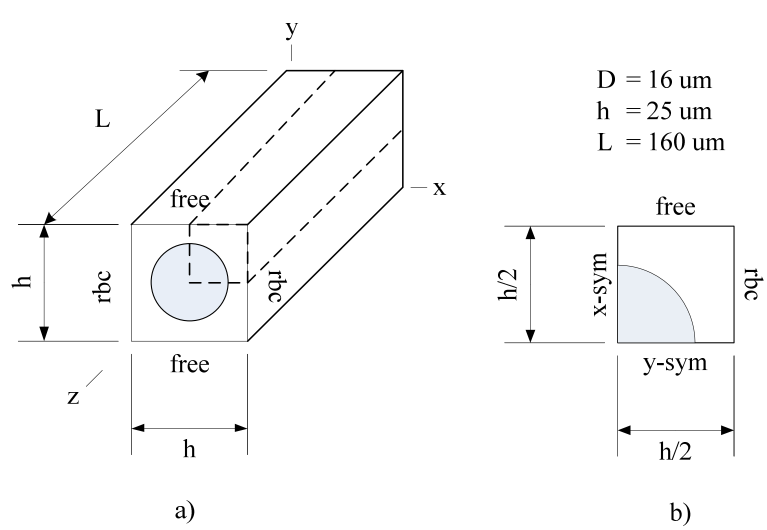

Figure 37. a) The M1 structural RUC; dashed lines indicate the location of the b) 1/4-symmetric structural RUC.

Applied Loads

For an nominal axial stress applied in the *z*-direction (σ_{33}^0), equilibrium is satisfied if a concentrated force F applied to the model is equal to the reaction force F_R generated at the back surface, as in the basic definition of stress shown in Equation 46.

$$\sigma_{33}^0 = \frac{F}{A} = \frac{F_R}{A} \qquad \text{Eq. (46)}$$

In order to provide a fair basis for comparisons between each model, the total reaction force in the axial direction (F_R) developed at the constrained back surface of each model must be the same – thus ensuring that each structural RUC carries the same load. Without the use of symmetry reductions, this requirement is expressed by

$$\sigma_{33}^0 = \frac{(F_R)_{M1}}{h^2} = \frac{(F_R)_{M2}}{h^2} = \frac{(F_R)_{M3}}{h^2} \qquad \text{Eq. (47)}$$

However, the use of reflectional symmetries results in a reduction to the FE model cross-sectional area, and the required reaction force must be similarly scaled. For example, in Model 1, the quarter symmetric model has a cross-sectional area of

$$A_{sym} = \frac{h^2}{4} = \frac{A}{4} \qquad \text{Eq. (48)}$$

Therefore, to ensure the same load is placed upon the symmetry model as would be placed on the "full" model, the required reaction force must also be scaled by a factor of 1/4, such that

$$F_{R_{sym}} = \frac{F_R}{4} \qquad \text{Eq. (49)}$$

therefore,

$$\sigma_{33}^0 = \frac{F}{A} = \frac{F_R}{h^2} = \frac{F_{R_{sym}}}{A_{sym}} \qquad \text{Eq. (50)}$$

Thus, for the same applied load, it becomes a simple matter to calculate the necessary reaction force that must be generated in each symmetric structural RUC.

In the current work, each model is subjected to the same remotely applied tensile loading,

$$\sigma_{33}^{0} = 128\ MPa \qquad \text{Eq. (51)}$$

therefore,

$$F_{applied} = F_R = \sigma_{33}^{0}\ A = 0.08\ N \qquad \text{Eq. (52)}$$

where $A = h^2 = 25\ \mu m^2$. Thus, for the symmetric models shown in Figures 33b, 35b, and 37b, the values below are obtained.

symmetric areas

$$A_{M1} = \frac{h^2}{4}$$

$$A_{M2} = \frac{h^2}{8} \qquad \text{Eq. (53)}$$

$$A_{M3} = \frac{h^2}{16}$$

symmetric reaction forces

$$F_{R_{M1}} = \frac{F_R}{4}$$

$$F_{R_{M2}} = \frac{F_R}{8} \qquad \text{Eq. (54)}$$

$$F_{R_{M3}} = \frac{F_R}{16}$$

In this work the tensile load condition is applied to the finite element mesh by placing a concentrated force at a reference node, acting in the +z-direction. Note that this reference node is not required to be connected to the rest of the meshed part. The displacement DOF of the reference node is then related to the displacements of other nodes using a linear constraint equation of the following form:

$$u_3^P - u_3^{ref} = 0 \qquad \text{Eq. (55)}$$

where *P* represents a single node or node set and *ref* indicates the reference node. Notice that the linear constraint equations are, therefore, applied in the same manner as the RBCs.

The fibers within each structural RUC are considered to be broken. Therefore, loading is applied to the matrix material only, at the forward (+z) surface of the RUC using the form of Equation 55. The fibers are left in an unloaded state. The nominal stress (σ_{33}^0) is applied by specifying a concentrated force at a reference node, which is distributed to the nodes in the matrix material only using the constraint given by Equation 55. The constraint between the reference node and the matrix nodes at the forward surface (belonging to the set *P*) guarantees that each node in the mesh connected to an element associated with the matrix material displaces in exactly the same manner – this is useful in the tensile loading condition in order to represent the symmetry plane that was previously illustrated in Figure 13. This is an important detail; notice that if a stress-based load had been directly applied to the matrix material, the nodes nearest to the fiber would displace less (due to the proximity of the stiffer fiber) and symmetry at the plane of the fiber break could not be accurately represented. The model boundary conditions (repeated from Figure 31) as well as the broken-fiber loading case are shown in Figure 38.

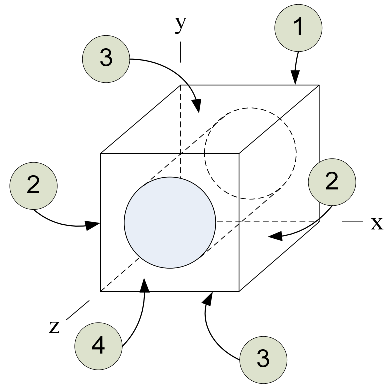

Figure 38. RUC Boundary conditions and applied loads.

In Figure 38, the numbers indicate the BC or loads corresponding to:

1. Rear face of RUC: no z-displacement
2. Left and right faces of RUC: RBC
3. Top and bottom faces of RUC: Free surface
4. Forward face of RUC: applied nominal tensile stress (applied to a reference node and distributed to the matrix material only, using the constraint given by Equation 55)

Constituent Material Properties

E-glass and a typical epoxy are used to simulate the fiber and matrix constituent materials, respectively, with typical values shown in Table 2 [**2**]. For simplicity, both fiber and matrix material models are assumed to be linear elastic and isotropic. Note that these values give a fiber/matrix modulus ratio of $E_f / E_m = 20$.

Table 2. E-glass and epoxy mechanical properties [**2**]

Material	Density, kg/m^3	Axial Modulus, GPa	Axial Poisson's Ratio
E-glass	2500	72	0.20
Epoxy	1200	3.5	0.30

Summary

In each model, the same fiber volume fraction ($V_f \approx 32\%$) within the well-defined volume of the structural RUC is ensured by increasing the number of fibers as the fiber diameter is decreased. A comparison of the different structural RUC is given in Table 3. The number of fibers required in each RUC can be calculated from Equation 2. The fiber-matrix surface area in each RUC can be calculated using Equation 3.

Table 3. Summary of structural RUC M1, M2, and M3

Model	Fiber Diameter, μm	Fiber Volume Fraction	No. of Fibers in h^2	Total Interfacial Surface Area in h^2L, μm^2
M1	16	0.3217	1	8 042.5
M2	8	0.3217	4	16 085.0
M3	4	0.3217	16	32 170.0

Figure 39 illustrates the geometry that may be obtained once reflectional symmetries are utilized, shown with respect to the original dimensions.

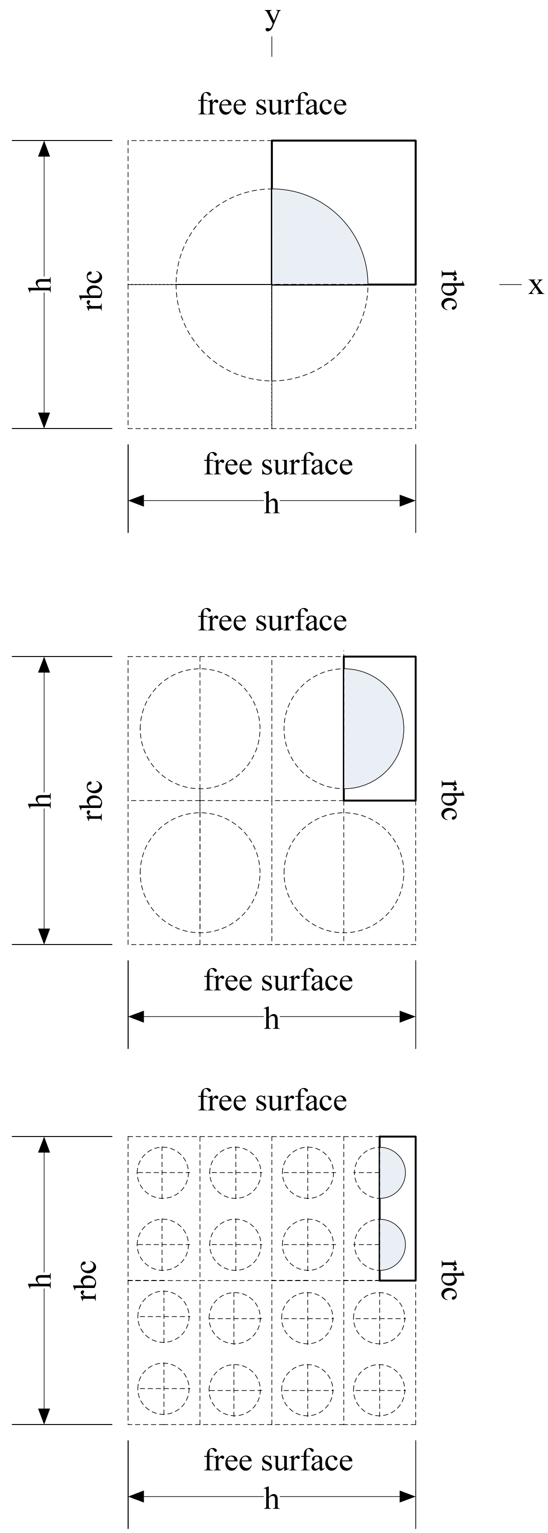

Figure 39. Structural RUC and symmetry model for a) Model 1; b) Model 2; c) Model 3.

RESULTS AND ANALYSIS

Overview

The general framework for the work conducted in this research is described in the previous sections. This framework consists of the core concepts:

1. The fiber-scaling method to increase the fiber-matrix interfacial area;
2. Micromechanics and homogenization theory;
3. Shear-lag stress transfer;
4. Interfacial damage and degradation using the cohesive zone model;
5. The necessity for the structural repeating unit cell;
6. Repeating boundary conditions.

To investigate the effects of fiber-scaling on the mechanical behavior of a composite material, this general framework is now applied to the analysis of the three structural repeating unit cell models described in the Model Development section. In the following sections, results from each model are grouped together according the type of analyses performed:

1. Shear-lag Analysis;
2. Interfacial CZM Analysis.

Shear-Lag Analysis

The shear-lag models described in this section detail the axial stress (σ) and shear stress (τ) distributions along the length of a broken glass fiber embedded in an epoxy matrix. The ineffective fiber length ($\ell_{0.9}$) is measured by determining the length required for 90% of the maximum load carrying capacity (σ_{max}) of the fiber to be recovered. The nondimensional ineffective fiber length ($\hat{L}_{inef}$) is evaluated by normalizing $\ell_{0.9}$ by the fiber diameter (*D*). The shear-lag models are also used to obtain the effective stiffness as the fiber diameter changes. Recall that τ is obtained at the fiber-matrix interface, while σ is obtained at the fiber center. The shear-lag analyses described in this section refer to the linear elastic response of a structural RUC model to boundary loads and the broken fiber load case, as described above. In the following cases, no interfacial damage is permitted. In a sense, this represents an infinitely strong interfacial bond. The implicit solver of the commercial finite element code, Abaqus/Standard, was used.

Model 1 Results

The axial stress (σ) and shear stress (τ) distributions along the fiber length are shown in Figure 40. As shown, the constrained boundary at the rear surface of the model is far from enough from the fiber break that no effect is made upon the stress field, and the stresses are allowed to fully develop along the fiber length. The maximum fiber axial stress and the maximum interfacial shear stresses are

$$(\sigma_{\max})_{M1} = 360.0\ MPa$$

$$(\tau_{\max})_{M1} = 68.9\ MPa$$

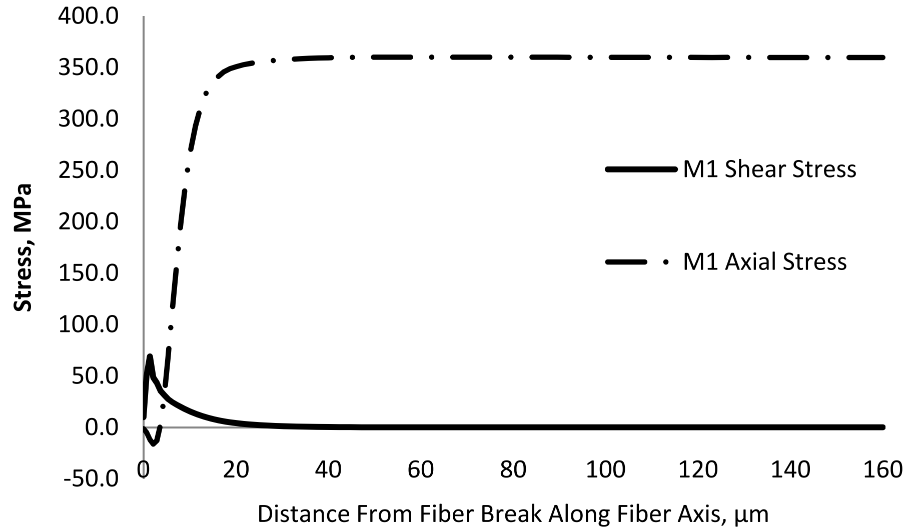

Figure 40. Axial and shear stresses along the length of the fiber in Model 1.

Figure 41 repeats this result for the first 30 μm from the fiber break. Here the ineffective fiber length can be clearly shown, where

$$(\ell_{0.9})_{M1} = 13.55\ \mu m$$

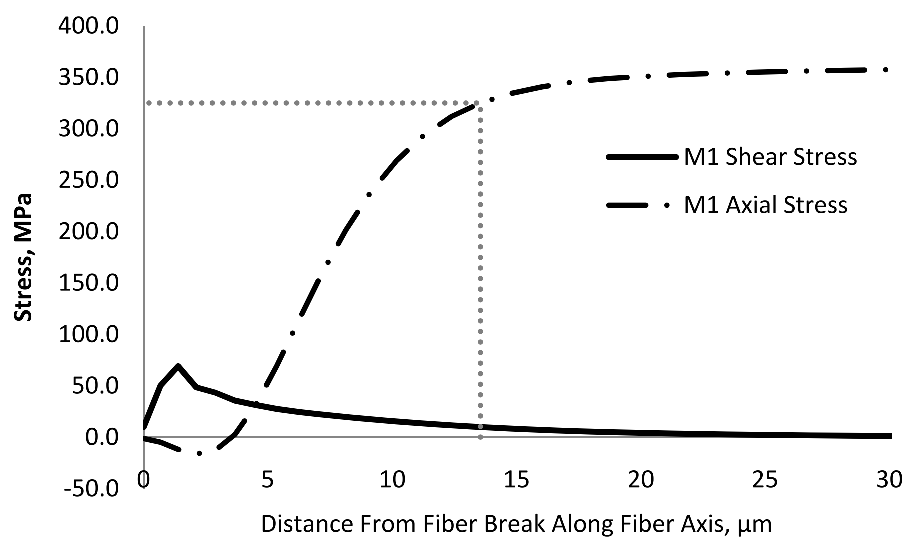

Figure 41. Axial and shear stresses over the first 30 μm of the fiber length in Model 1.

The results above are shown on the absolute stress scale in order to demonstrate the relative magnitudes of the shear and axial stresses. For clarity, the stresses may be normalized by their respective maximum values, as shown in Figure 42 over the first 30 μm of the fiber length. This allows one to see the relationship between the stresses as load is transferred from the matrix to fiber across the fiber-matrix interface more clearly.

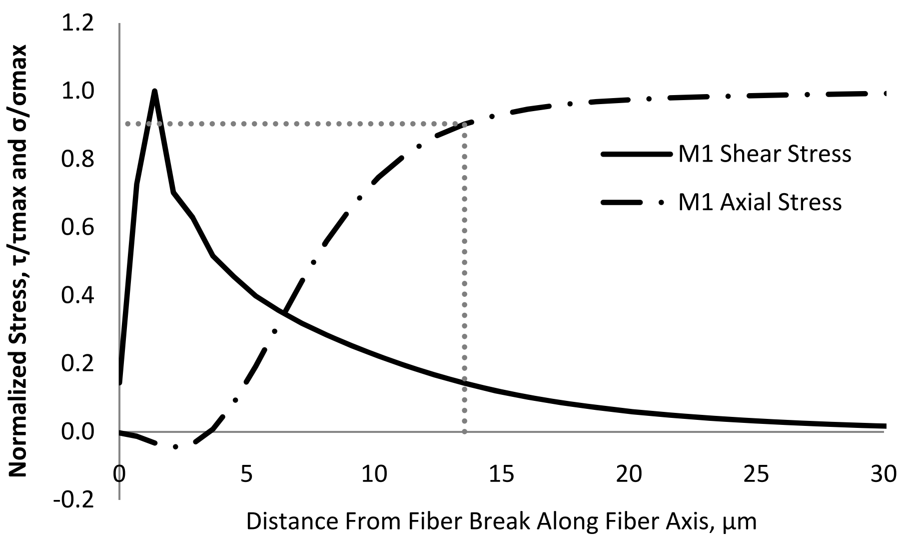

Figure 42. Normalized axial and shear stresses over the first 30 μm.

As one can see, the shear stresses at the interface (τ_{int}) quickly build and reach a peak value near the fiber break. As loads are transferred across the fiber-matrix interface the axial stress in the fiber (σ_f) builds, while τ_{int} simultaneously decreases. At the leading surface of the fiber, the stresses are zero because the fiber carries no load.

Interestingly, a compressive axial stress in the fiber is indicated by the "dip" shown in the figures above. This appears to be a physical result; it can be explained by considering the fact that near the fiber break, the matrix material carries the entire tensile load and is "pulling" on the fiber in the positive axial direction while the rest of the material pulls in the opposite direction. Due to the stiffness mismatch between matrix and fiber, however, the majority of the tensile load is quickly recovered by the stiffer fiber material as we progress along the fiber length away from the break. In addition, the matrix material forces the free surface of the fiber to be somewhat in compression as it bends slightly down into the open area in front of the fiber break. Contour plots of the axial and shear stresses near the fiber break are shown in Figure 43 and Figure 44, respectively. These were obtained from finite element analysis conducted in Abaqus.

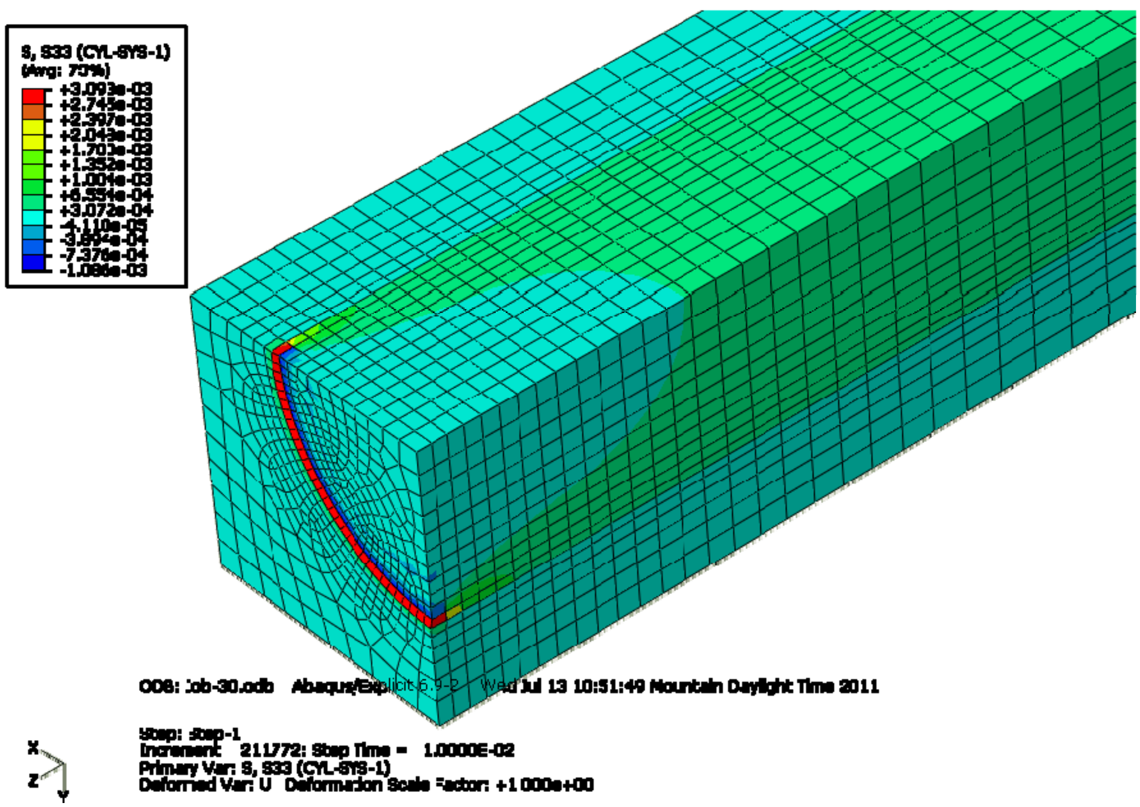

Figure 43. Contour plot of axial stresses near the fiber break.

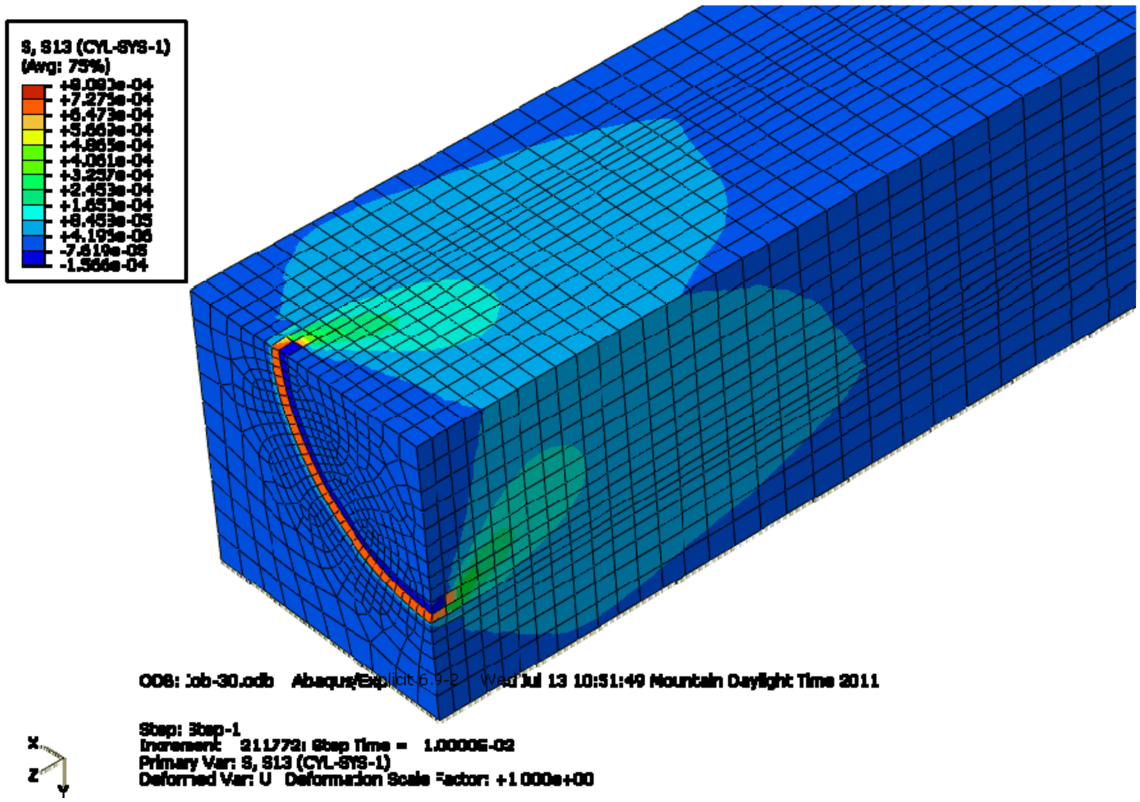

Figure 44. Contour plot of shear stresses near the fiber break.

<u>Model 2 Results</u>

The axial stress (σ) and shear stress (τ) distributions along the fiber length are shown in Figure 45, and for the first 30 μm only in Figure 46. These results are similar to those obtained from Model 1, however, it can be seen from the figures that the fiber axial stress is recovered more quickly, and the interfacial shear stress peaks at a lower value. The maximum fiber axial stress and the maximum interfacial shear stresses are

The ineffective fiber length is

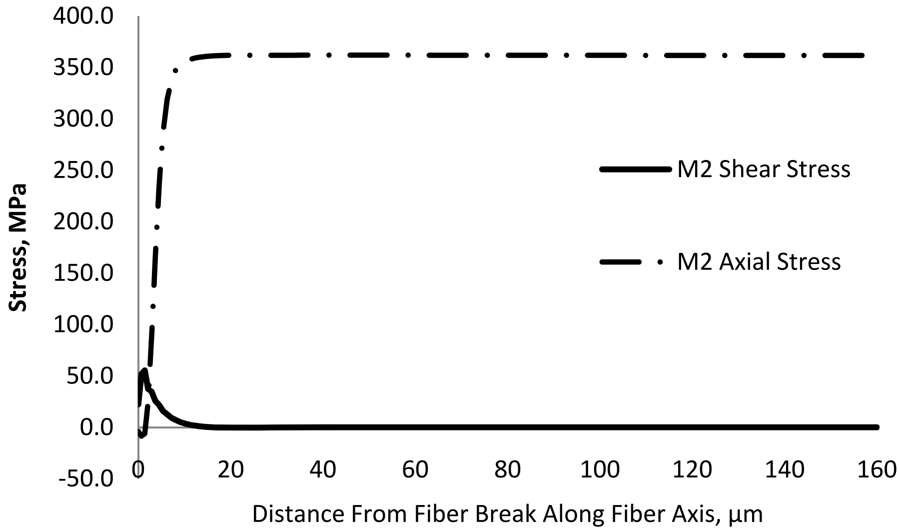

Figure 45. Axial and shear stress distributions for Model 2.

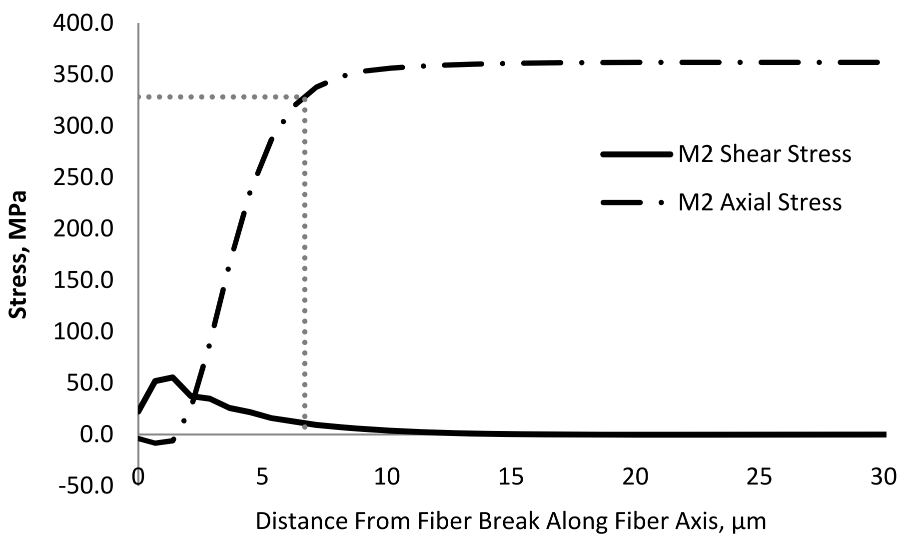

Figure 46. Axial and shear stresses over the first 30 µm of the fiber length in Model 2.

Again, for clarity the stresses may be normalized by their respective maximum values, as shown in Figure 47 over the first 30 µm of the fiber length.

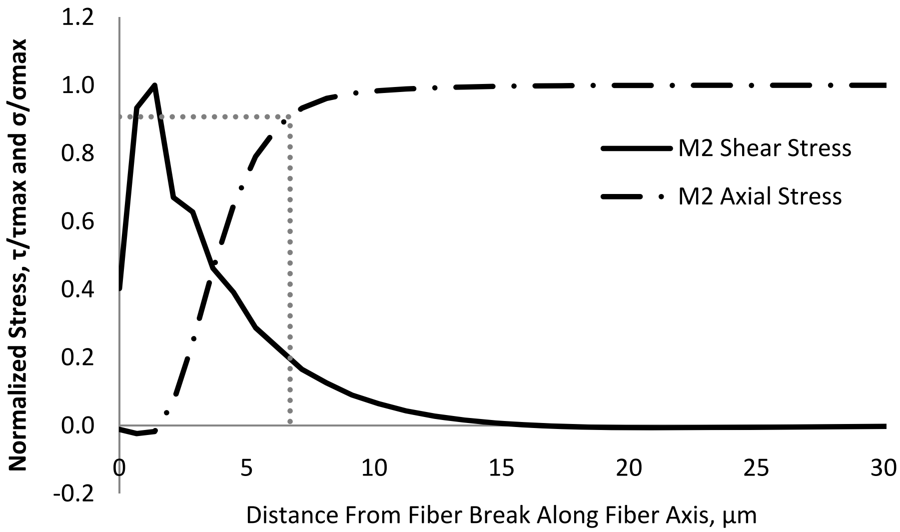

Figure 47. Normalized axial and shear stresses over the first 30 μm in Model 2.

<u>Model 3 Results</u>

The axial stress (σ) and shear stress (τ) distributions along the fiber length are shown in Figure 48, and for the first 30 μm only in Figure 49. These results are similar to those obtained from Model 1 and Model 2, however, the fiber axial stress is recovered even more quickly, and the interfacial shear stress peaks at an even lower value. The maximum fiber axial stress and the maximum interfacial shear stresses are

$$(\sigma_{\max})_{M3} = 364.6\ MPa$$

$$(\tau_{\max})_{M2} = 40.6\ MPa$$

The ineffective fiber length is

$$(\ell_{0.9})_{M1} = 3.26\ \mu m$$

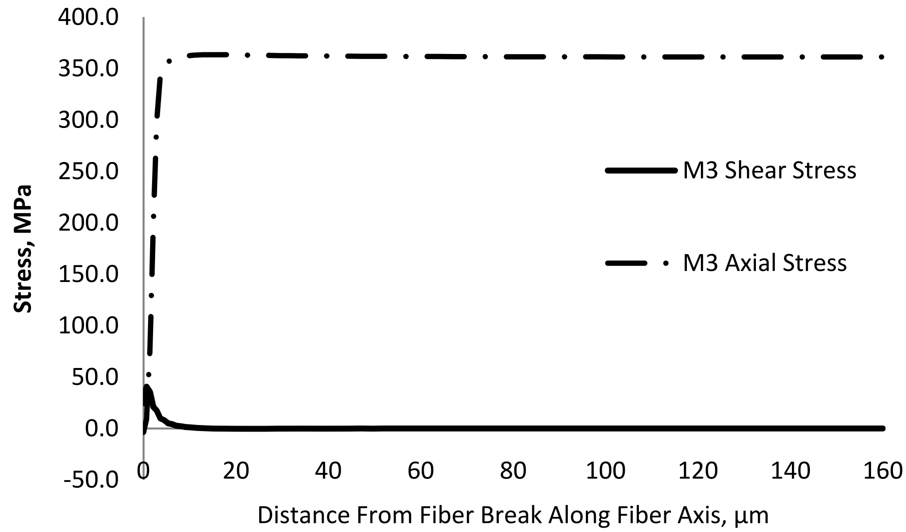

Figure 48. Axial and shear stress distributions for Model 3.

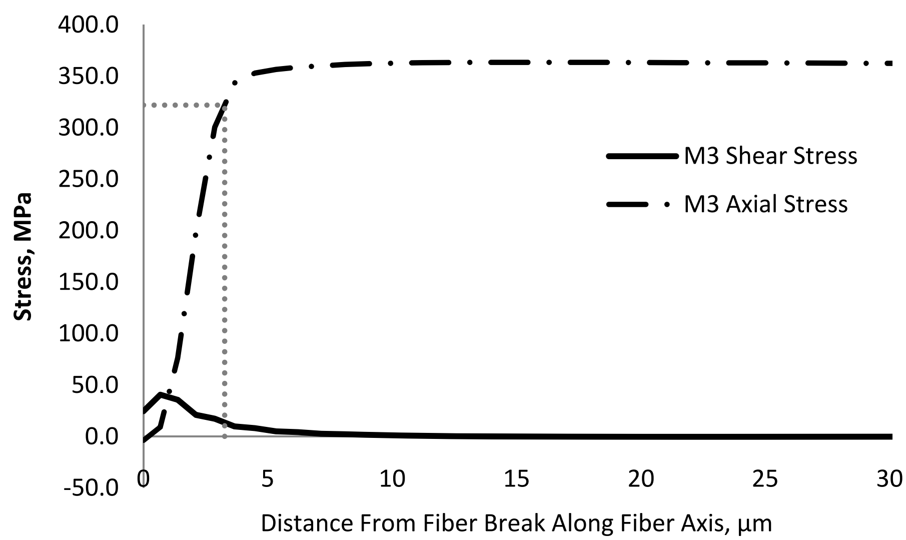

Figure 49. Axial and shear stresses over the first 30 µm of the fiber length for Model 3.

The normalized axial and shear stresses for Model 3 are shown in Figure 50 over the first 30 µm of the fiber length.

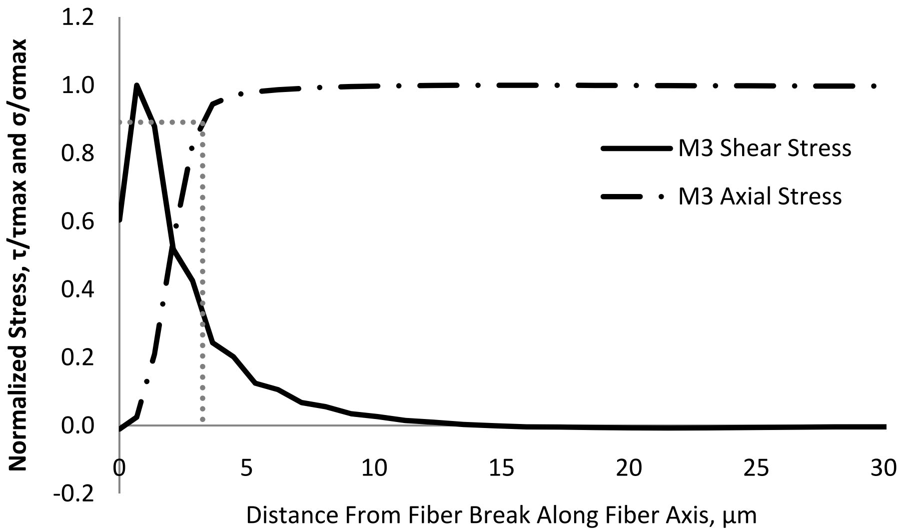

Figure 50. Normalized axial and shear stresses over the first 30 μm for Model 3.

Comparison of Shear-Lag Results

The axial stresses obtained from each model are shown together in Figure 51. In this figure it can be immediately seen that the magnitude of the axial stresses are quite similar – in fact, the greatest difference exists between Model 1 and Model 3, where the difference in magnitudes is approximately 1.3%. With further mesh refinement, this difference could likely be reduced, if desired.

The axial stresses for each model are repeated in Figure 52, for the first 30 μm only and where the ineffective fiber length $(\ell_{0.9})$ has been indicated by the dotted lines for each model. It can be seen that

$$(\ell_{0.9})_{M1} \approx 2(\ell_{0.9})_{M2} \approx 4(\ell_{0.9})_{M3}$$

This is an interesting result, and correlates well with the relative diameters of each model, which for Model 1, Model 2, and Model 3 are 16, 8, and 4 μm, respectively.

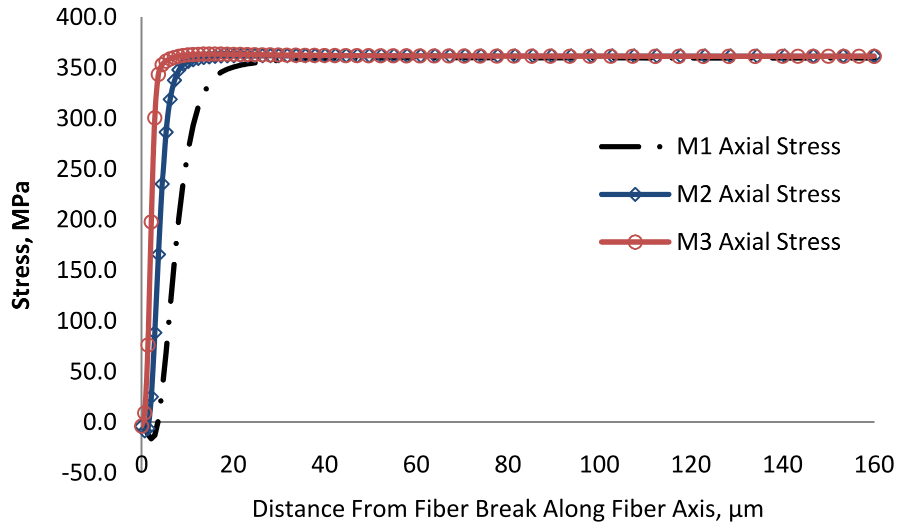

Figure 51. Comparison of axial stresses in each model.

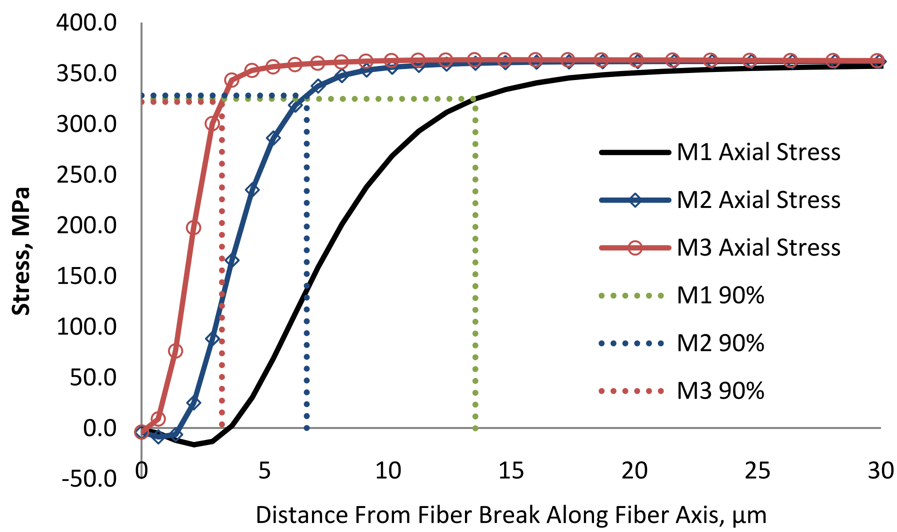

Figure 52. Comparison of axial stresses, showing the first 30 µm and the relative change in ineffective fiber length between each model.

In Figure 53, the axial stress is plotted where the horizontal axis is the normalized length scale, *z/D*. This represents the distance from the fiber break in diameters, and the nondimensional ineffective fiber length ($\hat{L}_{inef}$) can be easily compared. Notice that in each case, the nondimensional $\hat{L}_{inef}$ is approximately the same (again, likely the result of small discretization error). These results are summarized in Table 4.

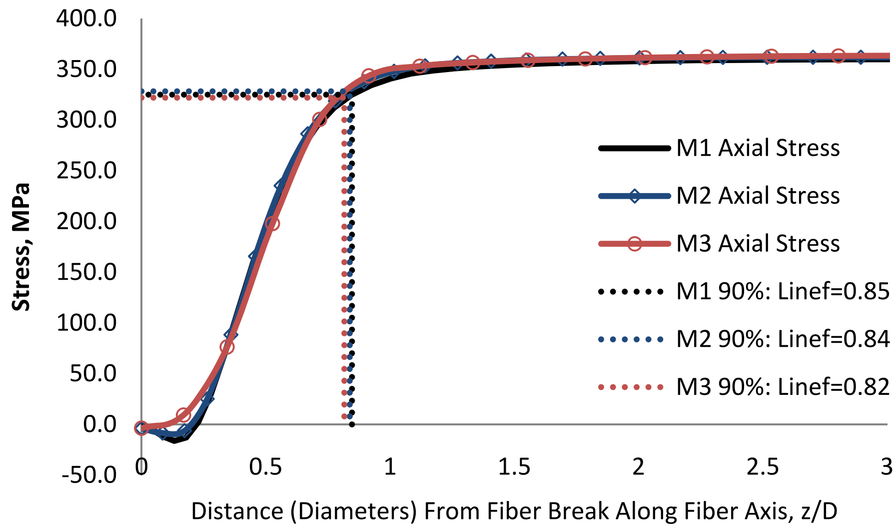

Figure 53. Comparison of axial stresses on the normalized length scale, *z/D*.

Table 4. Summary of ineffective fiber lengths for each model.

Model	$\ell_{0.9}$, µm	$\hat{L}_{inef}$, *z/D*
Model 1	13.55	0.85
Model 2	6.70	0.84
Model 3	3.26	0.82

The shear-lag analysis also provided insight into the effective stiffness for each model. The effective elastic stiffness for each system can be obtained from a load-displacement curve using the simple spring relation,

$$k_{eff} = \frac{load}{displacement} = F/\delta \qquad \text{Eq. (56)}$$

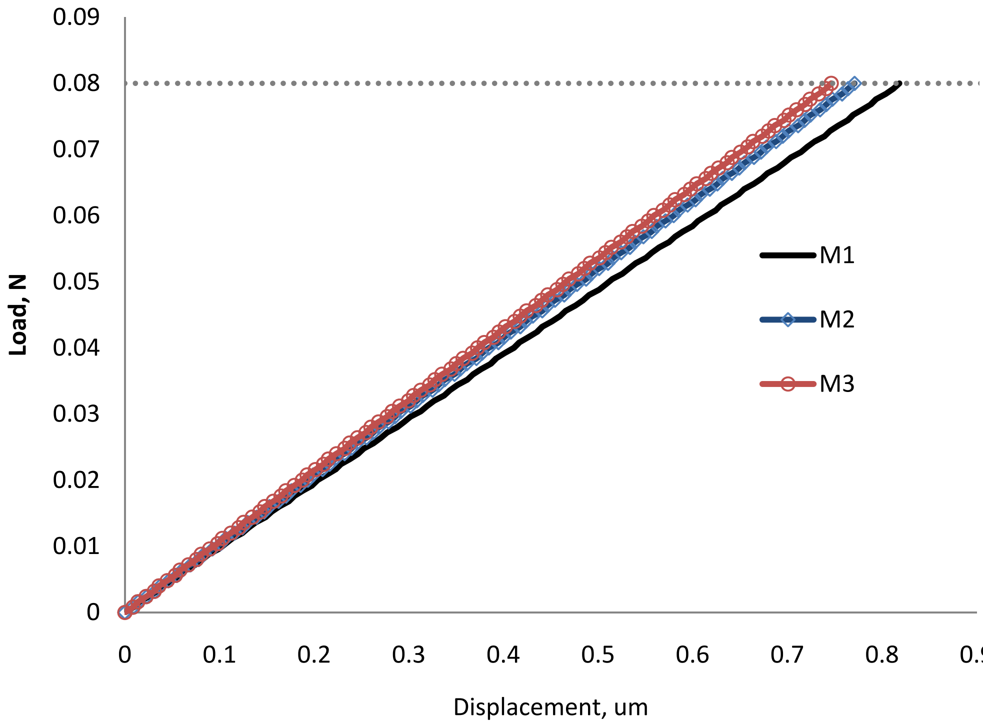

Figure 54. Load vs. Displacement curves for each model. The applied load is shown by the dotted line, where $F = 0.08$ N for each model.

Notice that Model 1, which used the largest diameter fiber ($D_1 = 16$ μm), experiences the greatest displacement for the same load. Model 3, which used the smallest diameter fiber ($D_3 = 4$ μm) experiences the smallest displacement for the same load. The total applied load (F), maximum displacement (δ), and the effective stiffness (k_{eff}) for each model are shown in Table 5.

Table 5. Comparison of load, displacement, and effective stiffness

Model	F (N)	δ (μm)	k_{eff} (kN/m)
Model 1	0.08	0.818	97.8
Model 2	0.08	0.771	103.8
Model 3	0.08	0.746	107.2

Cohesive Zone Model Damage Analysis

The CZM damage analysis described in this section refers to the response of a structural RUC model to boundary loads and the broken fiber load case. In this case, the cohesive elements are defined to exist in a zero-thickness interface at the fiber-matrix boundary, as shown in Figure 55.

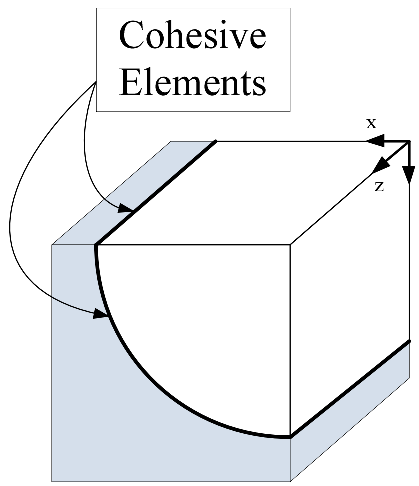

Figure 55. Location of cohesive elements at the fiber-matrix interface in the structural RUC models used in this work.

As discussed, the bilinear traction-separation relation is used in this work. The cohesive properties used for each element shown in Table 6 define this behavior for the current work. Recall, the initial penalty stiffness (K_0) is chosen to be large enough to prevent undesirable deformation across an interface before damage initiation, yet not so large that it results in ill-conditioning of the overall stiffness matrix. In addition, the interfacial cohesive strength (T_c) is chosen to represent the stress at which damage within a cohesive element initiates, while ultimate failure of an element occurs when the critical fracture energy (G_c) has been achieved.

Table 6. Cohesive element parameters

Property	Symbol	Value	Units
Initial Penalty Stiffness	K_0	5.0E+15	N/m^3
Interfacial Cohesive Strength	T_c	30.0	MPa
Fracture Energy	G_c	15.0	N/m
Density	ρ	1200	kg/m^3

At the risk of oversimplification, the cohesive parameters have been assumed to be the same in each direction. For example, the cohesive strength is assumed to be the same in the normal, first, and second shear directions (corresponding to the Mode I, Mode II, and Mode III fracture modes). Values have been chosen as a result of a review of the literature regarding interfacial fracture in glass/epoxy FRP composites. However, because this work is primarily concerned with the relative strengths of an FRP composite with regard to the fiber diameter used, the specific values used are relatively unimportant, as long as they are consistent between models.

Notice that the displacement at the onset of damage (δ_c) and at ultimate failure (δ_f) can be obtained using the shape of the bilinear traction-separation relation,

$$\delta_c = T_c/K_0 \qquad \text{Eq. (57)}$$

$$\delta_f = 2\, G_c/T_c \qquad \text{Eq. (58)}$$

Recall that G_c is taken to be the area under the T-δ curve. Because K_0 is chosen to be a large value, the deformation at the onset of damage is very small ($\delta_c = 0.006$ µm), while the deformation at failure is $\delta_f = 1.0$ µm. Normally, the area would be calculated using the difference found by ($\delta_f - \delta_c$), however the contribution of δ_c is negligible and is generally ignored.

The cohesive formulation chosen for this study utilizes the built-in framework provided by Abaqus. Use of the explicit solver in Abaqus/Explicit allowed solutions to be obtained for the case in which element degradation and deletion occurs, which pose significant problems for implicit solvers.

Load-Displacement Curves

The load-displacement curves for each model are shown in Figure 56. The applied load of 0.08 N is indicated by the dotted lines. Notice that as the fiber diameter decreases, a stiffer response is observed. In addition, Model 2 and Model 3 are able to sustain the applied load, while Model 3 experiences complete debonding well before the maximum load has been achieved.

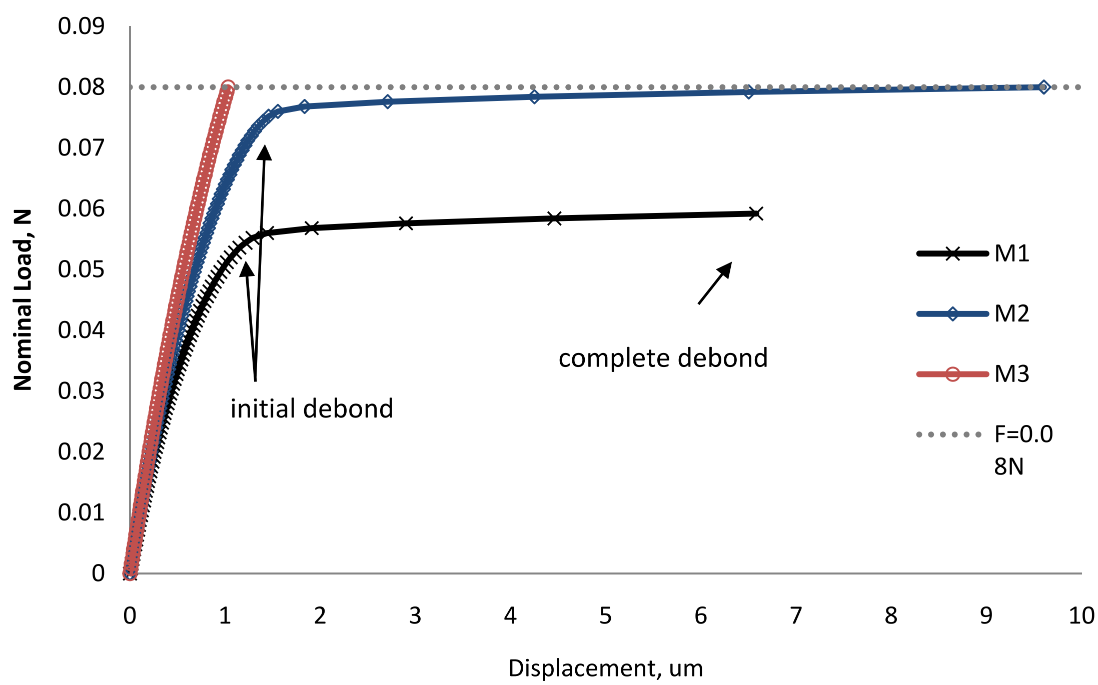

Figure 56. Load vs. Displacement for the cohesive zone damage models.

In each case, the response is slightly nonlinear up to the initial debond; once debonding occurs the behavior has a characteristic "hockey stick" shape. In fact, once the initial debond takes place in Model 1 and Model 2, very little extra loading may be sustained. In contrast, Model 3 does not experience any debonding.

Damage Initiation

The damage initiation criterion vs. displacement curve is shown in Figure 57 for each model, for the first element along the interface which reached the critical stress level. In the figure, a value of zero indicates an undamaged state, while a value of one indicates the initiation criterion (T_0) has been satisfied. Once satisfied, further loading and deformation results in material degradation and softening behavior of the element.

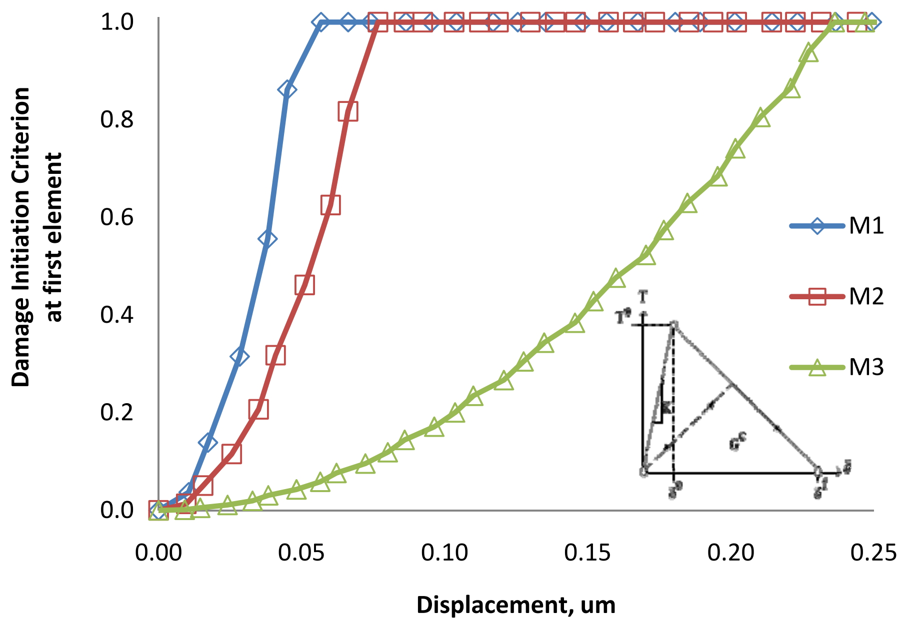

Figure 57. Damage Initiation Criterion at the first element to reach the critical load state.

This result shows that damage initiation occurs in Model 1 before Model 2, and Model 3 lags far behind.

Referring to the inset, notice that before the damage initiation criterion is met, a cohesive element behaves in a linear elastic manner. However, once T_c has been satisfied, the damage variable Φ begins to increase and the element stiffness is reduced as in Equation 33.

<u>Stiffness Degradation</u>

Figure 58 shows the growth of the damage variable (or the stiffness degradation variable) vs. displacement for the first element that reaches ultimate failure for each model. It can be seen that in both Model 1 and Model 2, the first element fails and crack growth begins. Model 3 does not reach the failure criterion at any point during loading for any element along the fiber-matrix interface. Using the inset for reference, recall that once the stiffness degradation, or damage variable, reaches a value of 1, the element has satisfied the fracture energy criterion, G_c, which is the area under the T-δ curve between the onset of damage (at the displacement of δ_c) and ultimate failure (at the displacement of δ_f).

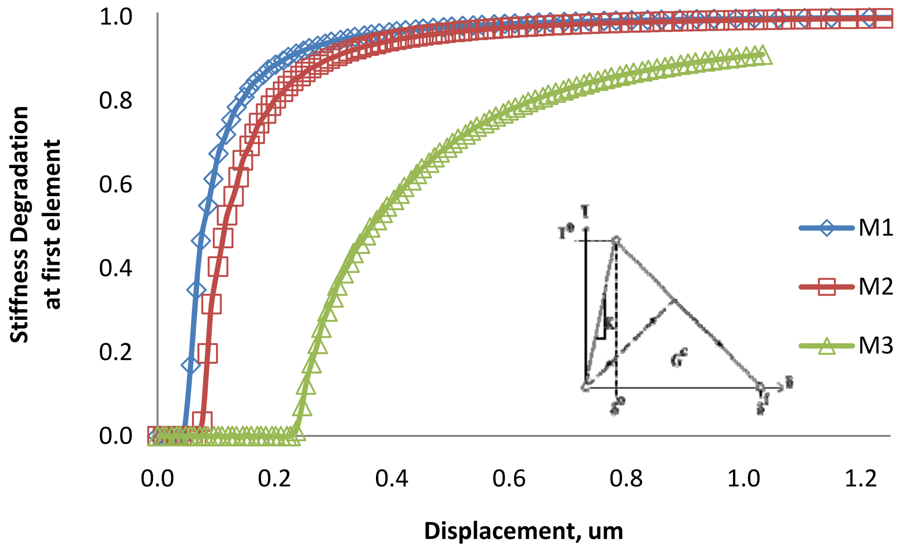

Figure 58. Stiffness degradation of the first element to fail in each model.

For clarity, this result is repeated in Figure 59, zoomed in on the region of interest. In this figure, it can be more easily seen that debonding begins at a displacement of

in Model 1 and Model 2. The degradation variable in Model 3 reaches a maximum of

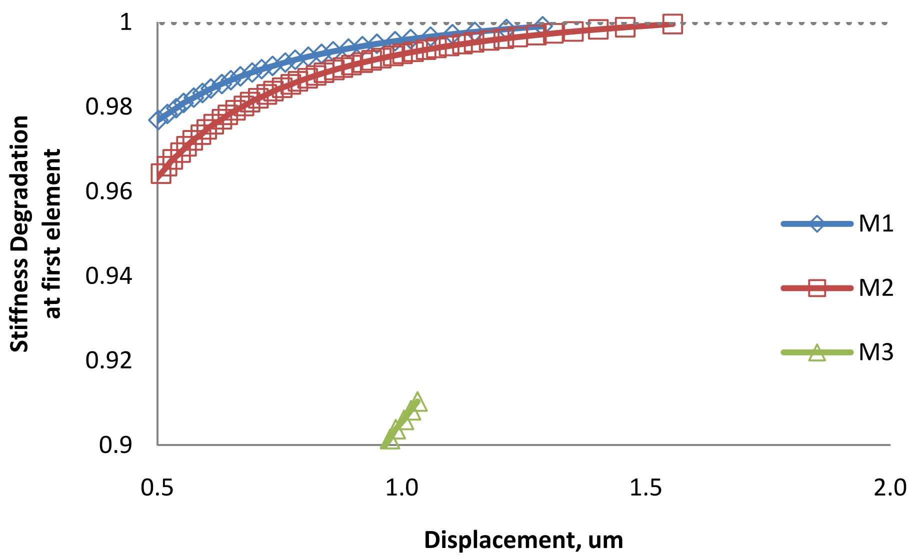

Figure 59. Zoomed in view of the stiffness degradation in the first element to fail.

From this figure, it can be seen that Model 3 experiences less critical damage than Model 2, which experiences less damage than Model 1. In addition, it should be noted that although Model 2 experiences interfacial debonding, it occurs at an applied load that is much larger than required for debonding in Model 1 (see Figure 56).

Therefore, it is useful to draw comparisons between each of the models by investigating the growth of the degradation variable related to the applied load, σ^0. The degradation variable along a path at the fiber-matrix interface for each model is shown in Figures 60-62, for 50%, 70%, and 100%, respectively, of the maximum applied tensile load.

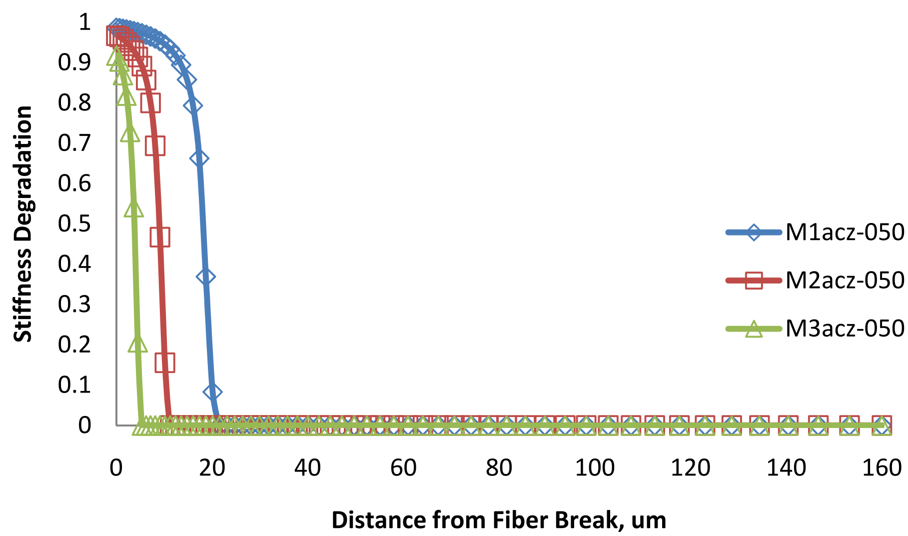

Figure 60. Stiffness degradation variable at 50% of σ^0 along a path on the interface. A value of 1 indicates a fully damaged element, while a value of 0 indicates the element is undamaged.

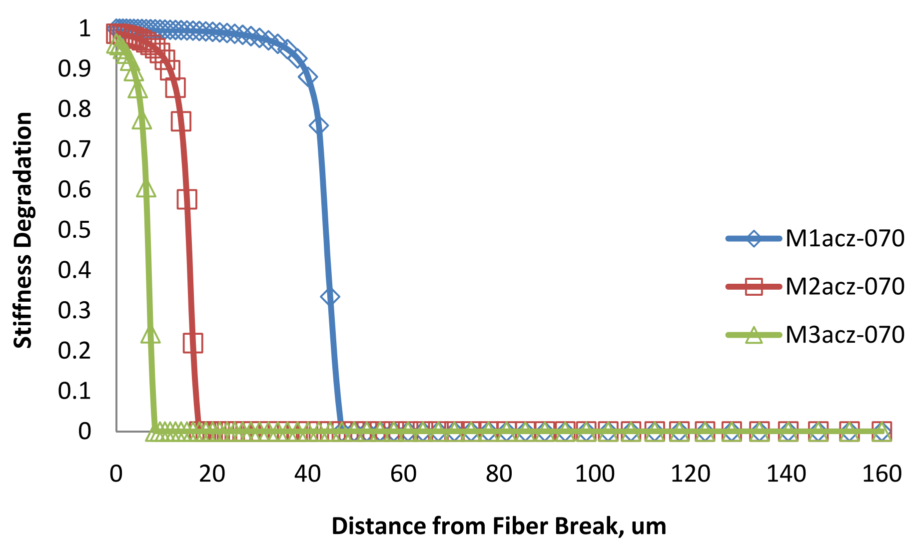

Figure 61. Stiffness degradation variable at 70% of σ^0 along a path at the interface.

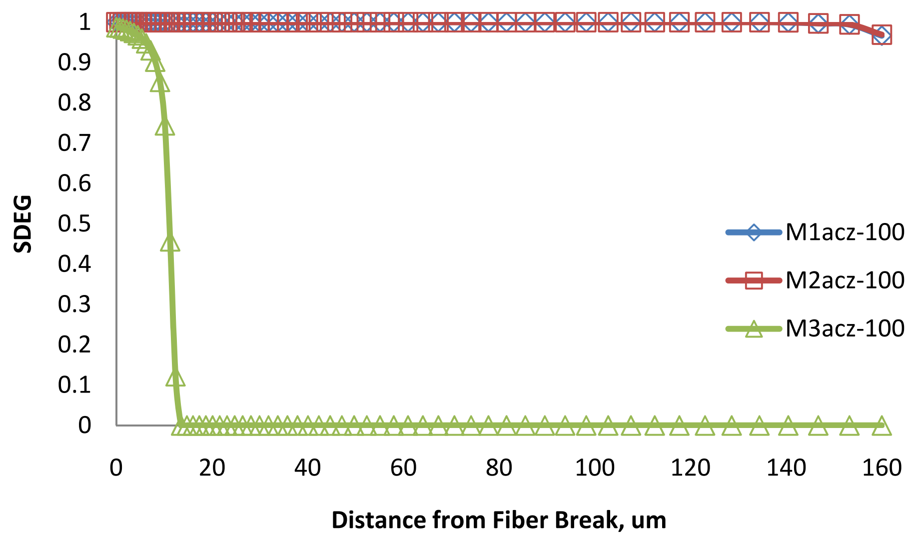

Figure 62. Stiffness degradation variable at 100% of σ^0 along a path at the interface.

As can be seen from the above figures, both Model 1 and Model 2 experience significant debonding along the length of the fiber. As already discussed, complete debonding in Model 1 occurs at a relatively low load. In comparison, Model 2 nearly debonds along the entire length, with the exception of a few elements near the rear constrained face of the model (which likely affected the state of the nearby cohesive elements), but manages to sustain the entire applied load of σ^0 = 128 MPa. Again, Model 3 is free from any debonding. In Figures 61-62, it can be seen that debonding growth occurs rapidly between 70% and 100% of the total applied load, particularly in Model 1. While damage does, indeed, reach critical levels along the length of Model 2, it evolves more slowly than in Model 1.

It is interesting to compare the behavior of the damage models to that of the shear-lag models. For the load-displacement curve seen in Figure 54 in the shear-lag section, the analogue for the damage model is as shown in Figure 63. Note that the behavior of the CZM is “softer” than the linear elastic models (denoted m1, m2, and m3 in the legend) as a result of nonlinear material degradation properties.

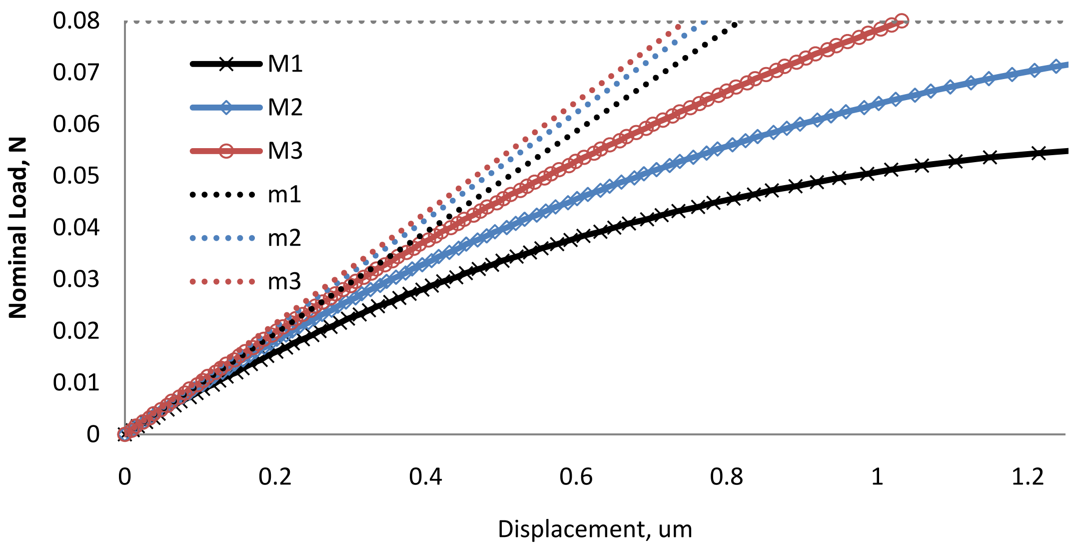

Figure 63. Load-displacement comparison of shear-lag and cohesive zone models.

SUMMARY AND CONCLUSION

Summary of Results and Discussion

Shear-Lag Analysis

The results from the shear-lag stress transfer analysis indicate that, for the same volume fraction and applied load,

1. The maximum axial stresses developed in the fibers are the same.
2. The maximum shear stresses developed at the fiber-matrix interface decreases as the fiber diameter decreases.
3. The ineffective fiber length ($\ell_{0.9}$) decreases as the fiber diameter decreases.
4. The nondimensional ineffective fiber length ($\hat{L}_{inef}$) is a constant ratio for the specific fiber volume fraction and modulus ratio tested.
5. The maximum displacement decreases as fiber diameter decreases.
6. The effective stiffness of the model increases as the fiber diameter decreases.

The result of (1) was expected, as it must be true in order to ensure that the same load is placed upon each model. Notice that in Model 2, four fibers together carry the same load as the single fiber in Model 1; similarly, in Model 3, 16 fibers together carry the same load as the single fiber in Model 1. Of course, each fiber in Model 2 and Model 3 carry one-quarter and one-sixteenth, respectively, of the total load F (or, the load carried by a fiber in Model 2 and Model 3 is less by a factor of $1/N$, where N is the number of fibers in the RUC. However, the stress in each fiber is the same as a direct result of the decreases in fiber diameter and the cross-sectional area (A), which scales by the same factor as the load which is carried by each fiber. For example, notice that $A_1 = 4A_2 = 16A_3$. Therefore, the maximum axial stress in each fiber is the same for each fiber in every model.

The result of (2) was an unexpected side effect from the fiber-scaling method. This result, however, appears to be an effect due to the increase in fiber-matrix interfacial surface area in the reduced-diameter models.

The result of (3) indicates that an increase in interfacial surface area (as a consequence of the fiber-scaling method) improves load transfer efficiency as the fiber diameter decreases. The result of (4) was quite interesting, indicating that for linear elastic models the nondimensional ratio of $\hat{L}_{inef} = \ell_{0.9}/D$ is a constant for the chosen volume fraction and modulus ratio. Note that the change in $\ell_{0.9}$ as a function of fiber volume fraction and the modulus ratio – and by extension, $\hat{L}_{inef}$ – is well documented in the literature already [**17**,**21**], and is not discussed in this work.

Finally, the results of (5) and (6) indicate that as the ineffective fiber length decreases, more of the stiffer fiber acts to resist loading; thus, the maximum displacement is reduced. This is another interesting, yet unexpected result.

Cohesive Zone Model Damage Analysis

The results from the CZM damage analysis indicate that, for the same volume fraction and applied load,

1. The initial response of each model is slightly nonlinear due to material degradation at the fiber-matrix interface.

2. Damage initiation occurs at higher nominal loads and greater displacements as the fiber diameter decreases.
3. Interfacial debonding occurs at higher nominal loads and greater displacements as the fiber diameter decreases. Model 1 experiences the debonding phenomenon first, followed by Model 2 (albeit, at much higher stresses). Model 3 does not debond at any point during the analysis.
4. Once the ultimate failure (the fracture energy, G_c) criterion has been met, the model can carry very little extra loads. The crack front extends easily once the initial element fails.
5. In comparison to the linear elastic shear-lag models, the response of the structure is “softer” as a result of the material degradation effects. The degree of the softening behavior decreases as fiber diameter decreases.

Every metric considered above indicates improved mechanical behavior and damage resistance in the models as the fiber diameter decreases. Therefore, these analyses point to the possibility that, for the same fiber volume fraction, improvements in the stiffness and load transfer efficiency of an FRP composite may be obtained by simply reducing the fiber diameter.

Future Work

The application of repeating boundary conditions to a structural repeating unit cell such as described in this work is an approach that warrants further examination.

Additional analysis could be done to assess the effects of RBCs on the results, e.g., plane stress vs. plane strain assumptions relative to the RBCs.

Conclusion

This investigation sought deeper insight into the effect that fiber diameter and the total fiber-matrix interfacial surface area have upon the mechanical properties and the damage resistance of an FRP composite material. It was found that by using the fiber-scaling method, the amount of fiber-matrix interfacial area increases as the fiber diameter decreases, while the fiber volume fraction and total mass of the composite remain the same. Results indicate that for a specified volume fraction and load condition, as the fiber diameter decreases the load transfer efficiency and effective stiffness of the broken fiber model increases. Also, as the fiber diameter decreases, the initiation of damage at the fiber-matrix interface occurs at greater stresses and subsequent growth of damage is less extensive. Thus, the results of this work show that for the same total mass, the performance and damage tolerance of composite materials may be enhanced simply by using smaller diameter fibers.

REFERENCES

[1] George J. Dvorak, Ed., *Inelastic Deformation of Composite Materials*. New York, NY: Springer-Verlag, 1991.

[2] Autar K. Kaw, *Mechanics of Composite Materials*, 2nd ed. Boca Raton, FL: CRC Press, Taylor & Francis Group, 2006.

[3] Stuart M. Lee, Ed., *Handbook of Composite Reinforcements*.: Wiley-VCH, 1992.

[4] Ben W. Kim and John A. Nairn, "Observations of Fiber Fracture and Interfacial Debonding Phenomena Using the Fragmentation Test in Single Fiber Composites," *Journal of Composite Materials*, vol. 36, no. 15, pp. 1825-1858, 2002.

[5] AGY, "AGY Technical Product Guide," 2009.

[6] Robert D. Cook, David S. Malkus, Michael E. Plesha, and Robert J. Witt, *Concepts and Applications of Finite Element Analysis*, 4th ed.: Wiley, 2002.

[7] "Military Handbook - MIL-HDBK-17-1F: Composite Materials Handbook, Vol. 1 - Polymer Matrix Composites Guidelines for Characterization of Strucural Materials," U.S. Department of Defense, 2002.

[8] Myer Kutz, Ed., *Mechanical Engineers' Handbook, Materials and Mechanical Design*, 3rd ed. Hoboken, NJ: Wiley, 2005.

[9] Marek-Jerzy Pindera, Hamed Khatam, Anthony S. Drago, and Yogesh Bansal, "Micromechanics of spatially uniform heterogeneous media: A critical review and emerging approaches," *Composites: Part B*, vol. 40, no. 5, pp. 349-378, July 2009.

[10] Martin H. Sadd, *Elasticity - Theory, Applications, and Numerics*, 2nd ed.: Academic Press - Elsevier, 2009.

[11] Shuguang Li, "On the Unit Cell for Micromechanical Analysis of Fibre-Reinforced Composites," *Proceedings: Mathematical, Physical and Engineering Sciences*, vol. 455, no. 1983, pp. 815-838, March 1999.

[12] Shuguang Li, "Boundary conditions for unit cells from periodic microstructures and their implications," *Composites Science and Technology*, vol. 68, pp. 1962-1974, 2008.

[13] Anthony Drago and Marek-Jerzy Pindera, "Micro-mechanical analysis of heterogeneous materials: Macroscopically homogeneous vs periodic microstructures," *Composites Science and Technology*, vol. 67, pp. 1243-1263, 2007.

[14] Tarek I. Zohdi and Peter Wriggers, *An Introduction to Computational Micromechanics*. Berlin, DEU: Springer, 2008.

[15] R. Hill, "Elastic properties of reinforced solids: some theoretical principles," *Journal of Mechanics, Physics, and Solids*, vol. 11, pp. 357-372, 1963.

[16] H.L. Cox, "The Elasticity and Strength of Paper and Other Fiberous Materials," *British Journal of Applied Physics*, vol. 3, no. 3, pp. 72-79, Mar. 1952.

[17] John A. Nairn, "On the Use of Shear-Lag Methods for Analysis of Stress Transfer in Unidirectional Composites," *Mechanics of Materials*, vol. 26, pp. 63-80, 1997.

[18] Z. Xia, T. Okabe, and W. Curtin, "Shear-lag versus finite element models for stress transfer in fiber-reinforced composites," *Composites Science and Technology*, vol. 62, pp. 1141-1149, 2002.

[19] J.M. Vazquez-Rodriquez, P.J. Herrera-Franco, and P.I. Gonzalez-Chi, "Analysis of the interface between a thermoplastic fiber and a thermosetting matrix using photoelasticity," *Composites Part A*, vol. 38, pp. 819-827, August 2006.

[20] N.M. Hossain, E.C. Milliren, K. Woo, and C.H. Jenkins, "The Effect of Fiber Diameter on the Strength of Lightweight Composites," in *51st AIAA/ASME/ASCE/AHS Structures, Structural Dynamics, and Material Conference*, Orlando, FL, 2010.

[21] N.M. Hossain, W.M. Peterson, K. Woo, and C.H. Jenkins, "Strength of flexible composites: Effect of fiber scaling," in *52st AIAA/ASME/ASCE/AHS Structures, Structural Dynamics, and Material Conference*, Denver, CO, 2011.

[22] H. Li, Y. Jia, G. Mamtimin, W. Jiang, and L. An, "Stress transfer and damage evolution simulations of fiber-reinforced polymer-matrix composites," *Materials Science and Engineering A*, no. 425, pp. 178-184, 2006.

[23] E.C. Milliren, "Nanocomposites: A Study of Theoretical Micromechanical Behavior Using Finite Element Analysis," Dept. of Mechanical and Industrial Engineering, Montana State University, Bozeman, MT 59717, MT, U.S.A., Master's Thesis 2009.

[24] W.M. Peterson, N.M. Hossain, K. Woo, and C.H. Jenkins, "Strength of flexible composites: damage tolerance in compliant unidirectional fiber reinforced composites," in *52nd AIAA/ASME/ASCE/AHS Structures, Structural Dynamics, and Material Conference*, Denver, CO, 2011.

[25] Normal E. Dowling, *Mechanical Behavior of Materials: Engineering Methods for Deformation, Fracture, and Fatigue*, 3rd ed. Upper Saddle River, NJ: Pearson Prentice Hall, 2007.

[26] Robert P. Wei, *Fracture Mechanics: Integration of Mechanics, Materials Science and Chemistry*. New York: Cambridge University Press, 2010.

[27] Rene de Borst, "Numerical aspects of cohesive-zone models," *Engineering Fracture Mechanics*, vol. 70, pp. 1743-1757, 2003.

[28] George Z. Voyiadjis and Peter I. Kattan, *Advances in Damage Mechanics: Metals and Metal Matrix Composites with an Introduction to Fabric Tensors*, 2nd ed. London, UK: Elsevier, 2006.

[29] SIMULIA, Abaqus Analysis User's Manual, v6.9, CH 28.5.

[30] A.A. Griffith, "The Phenomena of Rupture and Flow in Solids," *Philosophical Transactions of the Royal Society of London*, vol. 221, pp. 163-198, 1921.

[31] M. Elices, G.V. Guinea, J. Gomez, and J. Planas, "The cohesive zone model: advantages, limitations, and challenges," *Engineering Fracture Mechanics*, vol. 69, pp. 137-163, 2002.

[32] D.S. Dugdale, "Yielding of steel sheets containing slits," *Journal of the Mechanics and Physics of Solids*, pp. 100-104, 1960.

[33] De Xie and Anthony M. Waas, "Discrete cohesive zone model for mixed-mode fracture using finite element analysis," *Engineering Fracture Mechanics*, vol. 73, pp. 1783-1796, 2006.

[34] G.I. Barenblatt, "The mathematical theory of equilibrium cracks in brittle fracture," *Advances in Applied Mechanics*, vol. 7, pp. 55-129, 1962.

[35] A. Turon, C.G. Davila, P.P. Camanho, and J. Costa, "An engineering solution for mesh size effects in the simulation of delamination using cohesive zone models," *Engineering Fracture Mechanics*, vol. 74, pp. 1665-1682, 2007.

[36] A. Needleman, "An analysis of decohesion along an imperfect interface," *International Journal of Fracture*, vol. 42, pp. 21-40, 1990.

[37] V. Tvergaard, "Effect of pure mode I, II or II loading or mode mixity on crack growth in a homogeneous solid," *International Journal of Solids and Structures*, vol. 47, pp. 1611-1617, 2010.

[38] P.P. Camanho and C.G. Davila, "Mixed-Mode Decohesion Finite Elements for the Simulation of Delamination in Composite Materials," *NASA/TM-2002–211737*, pp. 1–37, 2002.